Genome-scale Model Constrained by Proteomics Reveals Metabolic Changes in *Streptomyces coelicolor* M1152 Compared to M145

Snorre Sulheim[1,2], Tjaša Kumelj[2], Dino van Dissel[1], Ali Salehzadeh-Yazdi[3], Chao Du[4], Gilles P. van Wezel[4], Kay Nieselt[5], Eivind Almaas[2,6], Alexander Wentzel[1], Eduard J Kerkhoven[7,8,*]

1. Department of Biotechnology and Nanomedicine, SINTEF Industry, Trondheim, Norway
2. Network Systems Biology Group, Department of Biotechnology and Food Science, NTNU - Norwegian University of Science and Technology, Trondheim, Norway
3. Department of Systems Biology and Bioinformatics, Faculty of Computer Science and Electrical Engineering, University of Rostock, Rostock, Germany
4. Microbial Biotechnology, Institute of Biology, Leiden University, Leiden, The Netherlands
5. Integrative transcriptomics, Center for Bioinformatics, University of Tübingen, Tübingen, Germany
6. K.G. Jebsen Center for Genetic Epidemiology, Department of Public Health and General Practice, NTNU - Norwegian University of Science and Technology, Trondheim, Norway
7. Systems and Synthetic Biology, Department of Biology and Biological Engineering, Chalmers University of Technology, Gothenburg, Sweden
8. Novo Nordisk Foundation Center for Biosustainability, Chalmers University of Technology, Gothenburg, Sweden

∗ Corresponding author. Email: eduardk@chalmers.se

Abstract

26

27 Many biosynthetic gene clusters (BGCs) in the genomes of environmental microorganisms

28 require heterologous expression in order to realize their genetic potential, including cryptic

29 and metagenomic BGCs. *Streptomyces coelicolor* M1152 is a widely used host strain for the

30 heterologous expression of BGCs, as it has been genetically engineered for this purpose via

31 the deletion of four of its native biosynthetic gene clusters (BGCs) and the introduction of a

32 point mutation in the *rpoB* gene that encodes the beta subunit of RNA polymerase. This

33 latter mutation was shown to have a strong positive impact on antibiotic biosynthesis via

34 processes that remain poorly understood. Therefore, a systemic understanding of the

35 consequences on cellular metabolism of the genomic changes of M1152 could greatly

36 contribute to this understanding. Here we carried out a comparative analysis of M1152 and

37 its ancestor strain M145, connecting observed phenotypic differences to changes in

38 transcript and protein abundance. Measured protein abundance was used to constrain an

39 amended genome-scale model (GEM) and to predict metabolic fluxes. This approach

40 connects observed differences in growth rate and glucose consumption to changes in central

41 carbon metabolism, accompanied by differential expression of important regulons. Our

42 results suggest that precursor availability is not limiting the biosynthesis of secondary

43 metabolites. This implies that alternative strategies could be beneficial for further

44 development of *S. coelicolor* for heterologous production of novel compounds.

Importance

46 This study provides the first systems description of *S. coelicolor* M1152, an engineered host

47 widely used for the heterologous expression of BGCs directing the synthesis of natural

48 products. By combining time-series proteomics and transcriptomics, batch fermentation

49   data and genome-scale modelling, we can connect observed phenotypes to known genetic

50   modifications and find extensive metabolic rewiring in the M1152 strain compared to the

51   wild-type stain M145. Our study indicates that the deletion of secondary metabolite

52   biosynthetic pathways thought to enhance precursor availability, only has a minor impact on

53   the ability of the modified strain to produced heterologous molecules. In contrast, the *rpoB*

54   mutation is likely responsible for the most dramatic changes in regulatory features and

55   precursor availability. The amended genome-scale model, reconstructed in an open-science

56   framework, allowed us to contextualize the transcriptional changes. This framework

57   facilitates further development by the research community in an organized manner,

58   including version control, continuous integration and quality control and tracking of

59   individual contributions.

Introduction

61   The bacterium *Streptomyces coelicolor* has been the *de facto* model actinomycete for the

62   production and regulation of antibiotics (1). Being known for over 100 years, the interest in

63   this organism predates the golden age of antibiotic research. With its complex life cycle,

64   featuring mycelial growth and differentiation, spore formation, programmed cell death and

65   the ability to produce multiple secondary metabolites, including calcium-dependent

66   antibiotic (CDA) and the conveniently coloured actinorhodin (Act, blue) and

67   undecylprodigiosin (Red, red), it has assisted greatly in our understanding how

68   streptomycetes sense their surrounding (2–6), activate their developmental cycle (7) and

69   regulate the production of antibiotics (8, 9). Further aided by the publication of its genome

70   sequence (10), the antibiotic coelimycin P1 (yellow), produced from the formerly cryptic

71   polyketide gene cluster known as *cpk*, was added to this list (11). Today, the widespread use

72   of *S. coelicolor* continues as a host for heterologous production of biosynthetic gene clusters

73   (BGCs) (12–17). Heterologous expression is a powerful strategy for novel compound

74   discovery from BGCs that are either natively silent or originate from an unculturable source

75   (18). Both are large untapped resources of microbial biodiversity, nowadays made evident

76   and accessible due to recent advances within the fields of metagenomics, molecular biology

77   and bioinformatics (19).

78   The efficiency of *S. coelicolor* as a heterologous production host relies on a metabolism that

79   has evolved to provide the necessary precursors to produce a broad range of complex

80   molecules. Many of these molecules are produced when the strain is experiencing nutrient-

81   limiting conditions that lead to growth cessation and complex re-modelling of its metabolism

82   (20). Metabolic switching in *S. coelicolor* M145 in response to phosphate and glutamate

83   depletion has previously been studied in detail at a wide variety of metabolic levels (1–3),

84   unravelling a complex sequence of switching events that ultimately lead to the biosynthesis

85   of the antibiotics CDA, Red and Act. The biosynthesis of coelimycin P1 occurs earlier than the

86   three other compounds in the growth cycle and appears to be independent of the major

87   metabolic switch (8).

88   To improve *S. coelicolor* M145 as a host for heterologous BGCs expression, strain M1146 was

89   created by the sequential deletion of its four major BGCs (*act, red, cda* and *cpk*) (13). This

90   should increase precursor availability for the production of a whole range of heterologous

91   products and provides a cleaner chromatographic background to easier identify novel

92   compounds. *S. coelicolor* M1152 is a derivative of M1146, that besides the deletion of the

93   four main BGCs bears the C1298T point mutation in the *rpoB* gene that encodes the beta

94   subunit of RNA polymerase. This mutation was shown to have strong positive effects on the

95   production of various antibiotics (13, 22). Up to now, M1152 is a preferred general

96   'superhost' for heterologous BGC expression (12, 16, 23–25) and is the starting point for

97   further strain development.

98   A hurdle in further development of *S. coelicolor* as a 'superhost' is the limited knowledge of

99   M1152 metabolism and its regulatory systems, even if some insight can be gained from

100   analysing snapshots of gene expression levels during regular time intervals of a batch

101   fermentation (26–30). Since enzymes are catalysing most metabolic transformations,

102   assessing protein abundance or gene expression contributes to the elucidation of metabolic

103   behaviour. Here, we therefore apply proteomics data as constraints (31) on a genome-scale

104   metabolic model (GEM) of *S. coelicolor* to reveal how proteome changes affect the

105   metabolic fluxes during the different stages of growth and development, and how the

106   metabolism of *S. coelicolor* M1152 differs from its parent strain, M145.

107   GEMs are both valuable resources of strain-specific knowledge, mathematical models able to

108   predict steady-state flux distributions, and frameworks for interpretation and integration of

109   different 'omics' data, e.g. transcriptomics and proteomics (32). The increased interest in

110   using genome-scale models of *S. coelicolor* is conspicuous. Since the first reconstruction in

111   2005 (33), five GEMs have been published (15, 34–37), including three in 2018: iKS1317 (15),

112   Sco4 (37) and iAA1259 (35). Additionally, as a model organism for the *Actinomycetes,* the

113   GEMs of *S. coelicolor* are frequently used as template for model development of closely

114   related strains (38), such as *S. clavuligerus* (39), *Saccharopolyspora erythraea* (40) and *S.*

115   *lividans* (41). The recent updates of the *S. coelicolor* GEM were developed in parallel by

116   different research groups: while all groups share the common interest of utilizing a high-

117   quality model for predictions and data analysis, the prevailing approach of independent

118   parallel development is inefficient. Additional to duplicating a considerable amount of work,

119   lack of common standards for documentation of progress and issues, evaluation of model

120   performance, as well as the use of different annotations makes it cumbersome to compare

121   and merge models.

122   To increase the rate and quality of model reconstruction, in this study two research groups

123   of the Sco-GEM community, responsible for two of the latest model updates (15, 37), have

124   joined forces to merge existing GEMs of *S. coelicolor* into one consensus-model that is

125   publicly hosted on GitHub and can be continuously updated and improved by all members of

126   the community. Hosting the model on GitHub has many advantages: (i) open access and

127   contribution; (ii) version control; (iii) continuous development and integrated quality control

128   with memote (42); (iv) new improvements released instantly (no publication lag time); and

129   (v) complete documentation of model reconstruction. Such an approach has historic

130   precedents: model reconstruction as a community effort has been a success for the human

131   GEM (43), baker's yeast (44–49) and Chinese Hamster Ovary cells (50). The recent

132   developments in *S. coelicolor* model and strain improvements in different research groups

133   prove that it is an opportune time now to join forces in the *Streptomyces* modelling efforts

134   as well.

Results
Improvement of Sco-GEM

137   We conducted a stepwise reconstruction of Sco-GEM, the consensus genome-scale

138   metabolic model of *S. coelicolor*, while tracking development using Git for version control

139   (**Figure 1A; Data Set S1, Tab 1**). Sco-GEM is the most comprehensive and highest quality

140   GEM of this organism (**Figure 1B**), comprising 1777 genes, 2612 reactions, 2073 metabolites

141   and a memote score of 77%, which is indicative of the overall model quality (42). Sco-GEM

142   features accuracy of 96.5% and 74.5% (**Figure 1C**) in predicting correct phenotypes for

143   growth environments and knockout mutants, respectively.

144   Sco-GEM has been reconstructed by curating the recently published iKS1317 model (15) to

145   include genes, reactions and metabolites from the equally recently published models

146   iAA1259 (35) and Sco4 (37). While the curations from iAA1259 were primarily related to

147   coelimycin P1, butyrolactone, xylan and cellulose pathways, the 377 reactions added to Sco-

148   GEM from Sco4 were scattered across a large range of different subsystems, covering both

149   primary and secondary metabolism (**Figure S1**).

150   Subsequent to merging the existing *S. coelicolor* GEMs, we performed a number of further

151   curations of the model: including improvement of annotations, both in terms of coverage

152   and number of different databases, e.g. KEGG (51, 52), BioCyC (53), ChEBI (54) and

153   MetaNetX (55). All reactions and metabolites have been given identifiers according to the

154   BiGG namespace (56), and all reactions are categorized into 15 different subsystems,

155   covering 128 different pathways.

156   The biomass composition was curated to reflect estimated levels of prosthetic groups that

157   are associated to cellular proteins. Proteomics data, as discussed below, were used to

158   estimate protein levels, while UniProt (57) provided annotations of proteins with prosthetic

159   groups, which was used to estimate overall prosthetic group levels (**Data Set S1, Tab 2**).

160   Reaction reversibility updated for almost a third of queried reactions

161   The determination of reaction directionality and reversibility is an important step in a GEM

162   reconstruction (58). However, the thermodynamic consistency of reactions was not

163   considered in previous *S. coelicolor* models. We calculated Gibbs free energy changes for 770

164   of the 2612 model reactions (**Data Set S1, Tab 3**) using eQuilibrator (59), and inconsistencies

165   in assigned reaction bounds transpired from a significant overlap of the range of Gibbs free

166   energies between reversible and irreversible reactions (**Figure 1D**). A relatively lenient

167   threshold of −30 kJ/mol was defined to classify a reaction as irreversible; with the intent not

168   to over-constrain the model (**Figure 1E**). The proposed changes in reversibility were

169   evaluated against growth and knockout data (15), discarding 59 of 770 of the proposed

170   reactions. Consequentially, the flux bounds of 273 reactions were modified, while all ATP-

171   driven reactions were manually curated and generally assumed irreversible, unless they had

172   an estimated positive change in Gibbs free energy or were known to be reversible. Examples

173   of this include nucleoside diphosphate kinase (60) and ATP synthase (61).

174   Curation of transport reactions

175   As transport reactions have previously not been extensively curated in *S. coelicolor* models,

176   we performed a thorough curation of transporters by querying various databases and BLAST

177   analysis as detailed in Materials and Methods. This culminated in adding 43 new transport

178   reactions and updating 39 of the 262 existing reactions in Sco-GEM (**Figure 1F; Data Set S1,**

179   **Tab 4**). The majority of the transporters comprises primary active transport proteins and

180   secondary carriers (46%), in accordance with previous work (62). Most primary active

181   transporters are ATP-binding cassette (ABC) transporters (30%), while proton symports

182   (30%) dominate the secondary carriers.

183   Development of the enzyme-constrained model EcSco-GEM

184   To include explicit constraints regarding enzymes catalysing metabolic reactions, the GECKO

185   formalism (31) was applied to introduce enzyme turnover rates (k_{cat}) and prepare the model

186   for integration of proteome data. The flux variability of the resulting enzyme-constrained

187   model (EcSco-GEM) is strongly reduced compared to the classic genome-scale model (**Figure**

188   **1G**), as infeasible solutions due to limitation in protein allocation are discarded, significantly

189   improving model predictions. From this, 17 time- and strain-specific EcSco-GEM models

190   were generated by incorporation of estimated growth-, secretion- and uptake rates, as well

191   as proteome data from cultivations that are detailed and analysed below.

192   Framework for further development of Sco-GEM by the community

193   The Sco-GEM model is hosted as an open repository as suggested by memote, a recently

194   developed tool for transparent and collaborative model development (42). The memote tool

195   is incorporated in the repository through Travis CI and tracks the model development on

196   every change of the model. Sco-GEM v1.2.0 achieved a memote-score of 77%, which is

197   superior to any previous model of *S. coelicolor* (**Figure 1B; Supplemental Information**).

198   Hosting Sco-GEM on GitHub with memote integration ensures continuous quality control

199   and enables public insight into all aspects of model reconstruction and curation: any user

200   can report errors or suggest changes through issues and pull requests. As contributions to

201   the model development are fully trackable and can therefore be credited fairly, Sco-GEM is

202   positioned as a community model that we envision to be continuously updated and widely

203   used by the *S. coelicolor* research community.

204   In the remaining parts of the Results section, we have applied Sco-GEM along with

205   transcriptome and proteome data, to study and compare the responses of *S. coelicolor*

206   M145 and M1152 to phosphate depletion on a systems level and for the first time provide

207   detailed insight into the distinct physiological features of engineered 'superhost' strain

208   M1152, which will be of value for its further development.

209

210   The enzyme-constrained model connects regulatory changes in *S. coelicolor* M145 in

211   response to phosphate depletion with the production of the major secondary

212   metabolites.

213   To evaluate whether the (Ec)Sco-GEM models can simulate behaviours of *S. coelicolor*

214   metabolism, we performed and analysed time-course sampled cultivations of secondary

215   metabolite producing strain M145 in the context of the generated models. For that purpose,

216   *S. coelicolor* M145 was cultivated in batch fermentations using standardized protocols

217   reported earlier (20). Cultures were sampled for 'omics data, as well as substrate utilization

218   and secondary metabolite measurements to identify regulatory, proteomic and metabolic

219   changes during the metabolic switch. The online and offline measurements showed that

220   phosphate depletion in the cultivation medium was reached approximately 35 hours after

221   inoculation. Shortly after, the culture growth ceased, and first Red and subsequently Act

222   were detected in the culture medium (**Figure 2A and 2B)**. Both D-glucose and L-glutamate

223   were consumed concomitantly, and their consumption continued after phosphate depletion,

224   while both remained in excess until the end of cultivation. Note that *Streptomyces* can utilize

225   intracellular phosphate storages after the medium is phosphate depleted (63). The RNA-seq

226   and untargeted proteomic data were analysed in the light of previous studies (8, 9) and were

227   in good agreement with data previously obtained from microarrays or targeted proteomics

228   (8, 34) (**Figure 2C and S2**). This confirmed the high reproducibility of the experiments across

229   independent cultivations and high reliability of the chosen cultivation and analytic

230   procedures (**Figure 2**).

231   The proteome data were incorporated into EcSco-GEM to yield time-specific metabolic

232   models of M145, giving insight on the changes occurring in the metabolic activity of different

233   pathways during batch cultivation. Metabolic fluxes were estimated using an unbiased

234   approach of random sampling, as alternative to optimization of a well-defined cellular

235   objective used in flux balance analysis (64). It is possible that *S. coelicolor* is wired to

236   maximize its growth rate prior to phosphate depletion, but after the metabolic switch, it is

237   difficult to define a clear cellular objective. We applied an approach that samples the

238   vertices of the solution space (65), and used their mean values to compare the metabolic

239   fluxes between the two strains and between different time points. The general overview

240   from **Figure 2D** is an initial validation of the model. It shows that the metabolic switch

241   induces a large shift in global gene expression (8) and predicts that the most drastic changes

242   in fluxes occur in response to phosphate depletion.

243   The response to phosphate depletion from the medium is achieved by a set of genes,

244   positively regulated by PhoP, that are involved in phosphate scavenging, uptake and saving

245   (66–68). The metabolic switch can be readily identified by the rapid upregulation of this

246   regulon after 35 hours of cultivation in M145 and 47 hours in M1152 (**Figure 2C**). PhoP also

247   negatively regulates nitrogen assimilation (69), which can partly explain the change in amino

248   acids metabolism after phosphate depletion. Indeed, from the RNA-seq data we find that

249   glutamate import, the glutamate sensing system *gluR-gluK* (70), *glnR* (71) and *glnA* are

250   downregulated immediately subsequent to phosphate depletion (**Figure S3**). Since PhoP is

251   also known to regulate negatively the biosynthesis of secondary metabolites, the switching

252   of its expression likely delays these pathways (69, 72). However, after 37 hours of cultivation

253   the upregulation of the *cda* and *red* genes was observed, whereas that of the *act* genes was

254   initiated at 41 hours (**Figure 2F**). Production of Red and Act was measurable in the culture

255   medium after 41 and 49 hours of cultivation, respectively (**Figure 2B**). The enzyme-

256   constrained models predict an immediate increase in fluxes through the biosynthetic

257   pathways for the four main compounds Act, Red, CDA and coelimycin P1 after the metabolic

258   switch (**Figure 2D**).

259   The onset of secondary metabolism is strongly correlated with an increase in oxidative

260   phosphorylation and a decrease in fatty acid biosynthesis in M145.

261   The metabolic switch was shown to be correlated with an enhanced degradation of

262   branched-chain amino acids (valine, leucine and isoleucine), an increase in oxidative

263   phosphorylation and a decrease in fatty acid biosynthesis (**Figure 2D and S4**). An active

264   oxidative phosphorylation relies on an active TCA cycle that generates reduced co-factors

265   whose re-oxidation by the respiratory chain generates a proton gradient that drives ATP

266   synthesis by the ATP synthase. The feeding of the TCA cycle requires acetyl-CoA, as well as

267   nitrogen. Nitrogen likely originates from degradation of glutamate and branched-chain

268   amino acids, whereas acetyl-CoA likely originates from glycolysis, as well as from the

269   degradation of these amino acids as previously demonstrated (73). Indeed, the model

270   predicts an increased flux through citrate synthase feeding acetyl-CoA into the TCA cycle

271   (**Figure S5A**). The predicted increase in oxidative phosphorylation is supported by the RNA-

272   seq data showing upregulation of enzymes belonging to the respiratory chain (**Figure S5B**).

273   This is consistent with the clear correlation previously reported between high ATP/ADP ratio,

274   resulting from an active oxidative phosphorylation, and actinorhodin production (74).

275   Furthermore, the consumption of acetyl-CoA by the TCA cycle to support the oxidative

276   metabolism logically impairs fatty acids biosynthesis (74).

277

278   The pentose phosphate pathway provides the main redox cofactor NADPH for polyketide

279   biosynthesis, as well as to combat oxidative stress, and its model-predicted flux increase

280   upon initiation of polyketide synthesis is in agreement with previous studies (75, 76). A clear

281   positive correlation was also noticed between the biosynthesis of alanine, aspartate and

282   glutamate, which are precursors for CDA and/or coelimycin P1 (**Figure 2D**) and the

283   biosynthesis of these antibiotics. Similar observations were made in the antibiotic-producing

284   *Amycolatopsis sp.* (77). Our EcSco-GEM model proved to be in good agreement with

285   previously reported findings, indicating that it is able to capture *S. coelicolor* metabolic

286   behaviour.

287   Model-assisted characterization of engineered *S. coelicolor* M1152 and its responses

288   to phosphate depletion.

289   As detailed above, EcSco-GEM shed a new light on the metabolic switch in secondary

290   metabolite producing strain M145. *S. coelicolor* M1152 (13) is a M145 derivative devoid of

291   the four major BGCs and bearing a point mutation in the *rpoB* gene. A better systemic

292   understanding of M1152 metabolism would benefit to its further development as a

293   performing host. To do so, a comparative analysis of gene expression levels and metabolic

294   fluxes was carried out in the strains M145 and M1152.

295   Batch cultivations of M1152 were performed using identical conditions and comparable

296   sampling regimes as for M145 reported above. This enabled a direct comparison of the two

297   strains at a systems level, revealing both expected and unexpected effects of the strains'

298   genetic differences (**Figure 3**). As anticipated, the products of the Cpk, CDA, Red, and Act

299   biosynthetic pathways were undetectable in M1152 (**Figure 3A**). As previously observed

300   (13), the growth rate of M1152 is reduced compared to M145 (0.15 h^{-1} vs 0.21 h^{-1} in the

301   initial exponential growth phase), delaying phosphate depletion by M1152 to 47 hours after

302   inoculation (**Figure 3A**).

303   The sampling time points for proteome and transcriptome were adjusted accordingly (**Figure**

304   **3B**), enabling pairwise comparison of measurements between the two strains. Genes

305   responsive to phosphate depletion, members of the PhoP regulon (8), were used to align the

306   different sample datasets for M145 or M1152 (**Figure 3C**). Interestingly, most of the

307   responses of M145 to phosphate depletion were retained in M1152 (**Figure 3D**). Principle

308   component analysis of the proteome data confirms high consistency between corresponding

309   biological replicates and incremental changes between sample points for both M145 and

310   M1152 (mainly explained by PC1: 18.6% variance, **Figure 3E**). A clear strain dependent

311   clustering of the data (PC2: 15.5% variance) indicates global significant differences at the

312   protein level. EcSco-GEM was subsequently used to predict metabolic changes in M1152

313   (**Figure 3E**).

314   The different glutamate and glucose consumption rates of M145 and M1152 (**Figure 4A and**

315   **4B**) resulted in substantial metabolic differences between the two strains prior to phosphate

316   depletion. During cultivation on SSBM-P medium, where glutamate is the sole nitrogen

317   source, glucose and glutamate are co-consumed. M1152, as M1146 (74), has a reduced

318   specific glucose uptake rate compared to M145. It thus obtains a larger share of its carbon

319   from glutamate (**Figure 4A and 4B**) and has consequently also a higher nitrogen availability

320   than M145. A reduced flux through glycolysis has also been reported previously for strain

321   M1146 (78). This might be an effect of the predicted increased concentration of ATP in

322   M1146 compared to M145, which inhibits glucose uptake and phosphofructokinase (74, 78).

323   Since Act was proposed to act as an electron acceptor reducing the efficiency of the

324   oxidative phosphorylation, it is suggested that the lack of Act in M1146 causes the elevated

325   ATP levels (74). However, we find the largest difference in glycolytic flux at early time points,

326 prior to phosphate depletion and Act production in M145, proving that Act itself cannot

327 explain this observation.

328 The EcSco-GEM predicts the consequences of the reduced glucose uptake of M1152 on its

329 central carbon metabolism (**Figure 4C**). A less active glycolysis in M1152 than in M145 leads

330 to a lower carbon flow towards acetyl-CoA and thus lower excretion of acetate compared to

331 M145 (**Figure 4B**). Furthermore, EcSco-GEM reveals an increased flux from glutamate to

332 alpha-ketoglutarate. Indeed, a fraction of the pool of oxaloacetate might be converted into

333 alpha-ketoglutarate by aspartate transaminase to feed the TCA cycle. The rest might be

334 converted into phosphoenolpyruvate (PEP) by PEP carboxykinase for gluconeogenesis, since

335 PEP carboxykinase was shown to carry higher fluxes in M1152 than in M145 (**Figure 4C**).

336 Since recent studies have demonstrated a reverse correlation between antibiotic and

337 triacylglycerol biosynthesis in *S. lividans* and *S. coelicolor* (74, 79), one can speculate that the

338 acetyl-CoA/malonyl-CoA units yielded by glycolysis for the biosynthesis of antibiotics in

339 M145 are being used for enhanced growth and/or fatty acids and TAG biosynthesis in

340 M1152. However, this is likely not the case, as M1152 has rather a reduced growth rate

341 compared to M145, and fatty acid biosynthesis remains downregulated after the switch

342 (**Figure 5**). It is noteworthy that the flux toward this acetyl-CoA/malonyl-CoA sink is still 3- to

343 6-fold larger than the total flux going into secondary metabolite biosynthesis. We thus

344 propose that together with enhanced nitrogen availability, acetyl-CoA made available from

345 the deletion of these BGCs is used to feed the TCA cycle to support the oxidative metabolism

346 in M1152. This would generate oxidative stress whose toxic effects might be responsible for

347 the growth delay of this strain.

348   Transcriptome analysis reveal differential expression of global regulators

349   While the proteome data are an integral part of the EcSco-GEM models, RNA-seq data were

350   used to both verify the trends and to gain further insights in the regulatory changes that are

351   not captured by the metabolic models. As the proteomic data, the RNA-seq data showed

352   large global differences between M1152 and M145, revealing 499 differentially expressed

353   genes with a significance threshold of p<0.01.

354   Unsupervised clustering of the significantly changed genes reveal differences in regulatory

355   systems related to redox regulation, signalling and secondary metabolism. The significantly

356   changed genes were clustered into 7 groups with K-means clustering, with clusters 1-3

357   containing genes that are upregulated in M1152 compared to M145 and clusters 4-7 vice

358   versa (**Figure S6A and Data Set S1, Tab 5**). A Gene Ontology (80, 81) enrichment analysis of

359   the seven clusters was conducted to identify upregulated processes in each of the two

360   strains (**Figure S7**, **cf. Figure S6A**).

361   The enriched processes upregulated in M1152 point to increased oxidative stress (**Figure S7**):

362   antioxidant and peroxidase activity (SCO2633 [sodF]; SCO4834-35) in addition to

363   biosynthesis of carotenoid (SCO0185–SCO0188), a known antioxidant (82, 83). The putative

364   proteins within the cytochrome-P450 family (SCO7416–SCO7422) found in cluster 1 might

365   also be linked to increased oxidative stress (84), but also to oxidation of precursors used for

366   the synthesis of macrolides (85). Indeed, by comparing the time series expression levels for

367   genes related to oxidative stress we observe that the majority of genes related to oxidative

368   stress are upregulated in M1152 (**Figure 6**). These changes correlate to a more active

369   oxidative metabolism and TCA cycle as predicted by Ec-ScoGEM (**Figure 4**).

370   In cluster 2 we find *scbA* (SCO6266) and its downstream gene *scbC* (SCO6267), which stands

371   out by being almost 6-fold upregulated in M1152. This high expression level is likely due to

372   the deletion of *scbR2* (SCO6286), the last gene selected to be part of the *cpk* BGC (86).

373   Besides regulation of the *cpk* cluster, ScbR2 binds upstream of several global regulators of

374   development and secondary metabolism, including AfsK, SigR, NagE2, AtrA, AdpA and ArgR

375   (87). It also acts together with ScbR to regulate ScbA, which produces the y-butyrolactone

376   SCB1. However, when looking at the genes regulated by ScbR (87), we only observe a clear

377   difference in expression for genes regulated by AfsR (phosphorylated by AfsK) (88, 89), while

378   this is not the case for genes regulated by ArgR, AdpA or ScbR itself (**Figure S5C-F**).

379   Amongst the genes upregulated in M145, in cluster 4 we find genes related to the redox

380   regulated transcription factor SoxR (90), and a similar pattern is observed for the entire SoxR

381   regulon (**Figure S6B**). SoxR is known to react directly to the presence of actinorhodin (91,

382   92), and indeed, in M145 this group of genes follows the production profile of actinorhodin,

383   while their expression remains low in M1152 since Act is not produced. The benzoquinone

384   Act, as electron acceptor, is thought to reduce respiration efficiency and thus energy charge

385   as well as to combat oxidative stress (74). Consistently, the RNA-seq data revealed that the

386   ATP-synthase gene cluster (SCO5366–SCO5374) was upregulated almost 2-fold in M1152

387   compared to M145, most prominently in the stationary phase during Act production (**Figure**

388   **S6C**). This agrees with observations in the M1146 strain (78). Cluster 4 also contains the

389   genes directly up- and downstream of the deleted actinorhodin BGC in M1152 (SCO5071–

390   SCO5072, encoding 3-hydroxyacyl-CoA dehydrogenase, and SCO5091–SCO5092, encoding a

391   two-component flavin-dependent monooxygenase system) (93). In clusters 5, 6 and 7 we

392   find genes with reduced expression in M1152, and the enriched processes are related to

393   cellular and iron ion homeostasis, development, signalling and morphology. This

394   corresponds to the delayed sporulation observed for M1152 (13).

Elevated expression of ribosomal proteins in M1152 after phosphate depletion

396   An increased transcription of genes encoding ribosomal proteins could be observed in

397   M1152 after phosphate depletion (**Figure S6D**). The *rpoB* mutation of the RNA polymerase

398   present in M1152 is thought to induce a conformational change mimicking the binding of

399   guanosine tetraphosphate (ppGpp) to this enzyme (22). ppGpp is synthesized in response to

400   nutritional stress and reduces the transcription of genes related to active growth, such as

401   genes encoding ribosomal RNAs and ribosomal proteins (94), whereas it up-regulates those

402   involved in development/differentiation and antibiotic production (95, 96). In consequence

403   the up-regulation of ribosomal proteins was unexpected in M1152, especially since the

404   expression of the ppGpp regulon was not found to be significantly changed in M1152 (**Figure**

405   **S5G and S5H**). However, since high nucleoside triphosphate levels are known to have a

406   positive impact on ribosome synthesis (97), we hypothesize that the higher ATP content of

407   M1152 compared to M145, after phosphate depletion, may be responsible for the

408   differences in expression of ribosomal proteins. Such difference in ribosomal protein

409   expression is mainly seen in the antibiotic production phase and correlated with production

410   of Act in M145, which has a negative impact on the energetic state of the cell (74).

Reduced production of the polyketide germicidin in M1152

412   It is usually thought that removal of sinks consuming valuable precursors improves the

413   ability of a strain to produce heterologous metabolites requiring these precursors for their

414   biosynthesis. It was therefore unexpected that the production rate (in ng ml^{-1} hour^{-1}) of the

415   polyketides germicidin A and B (98), autologous to both M145 and M1152, was reduced by

416   92% and 82% for germicidin A and B in M1152, respectively (**Figure 7**). This could be

417   explained by the more active oxidative metabolism of M1152 compared to M145. In M1152

418   the pool of acetyl-CoA would thus be used to feed the TCA cycle rather than be used for

419   germicidin biosynthesis.

420   To further understand the cause of the reduced production in M1152, we also measured the

421   production of germicidin in the intermediate strain M1146 (**Figure 7, Figure S6E**), which does

422   not feature the *rpoB* mutation but is missing the 4 BGCs also deleted in M1152 (13). The

423   production rate of germicidin A and B in M1146 was found to be reduced by 27% and 25%,

424   respectively, compared to M145. This demonstrates that, while the removal of BGCs may

425   influence polyketide production, a strong reduction appears to be assignable to the *rpoB*

426   mutation in M1152.

Discussion

428   In this work, we carried out a multi-omics study to compare the metabolic changes of

429   *Streptomyces coelicolor* M145 and the BGC-deletion mutant M1152 during batch

430   fermentation. The defined cultivation medium used in this work was chosen because it

431   supports sufficient growth and a delayed, well-defined onset of secondary metabolism,

432   necessary to study the metabolic switch (20). We aimed at defining the metabolic features

433   differing between the two strains, both during exponential growth and stationary phase

434   after phosphate depletion.

435   To achieve this from a systems biology perspective, we combined time-course sampled

436   cultivation and transcriptome analysis with enzyme-constrained genome-scale models

437   generated with proteome data. Such genome-scale models are extensively used to connect

438   transcriptome- and proteome data to metabolic fluxes. Leveraging metabolic simulations to

439   contextualize transcriptional changes is mainly impacted by the quality of the computational

440   model used. Here, two teams joined efforts to improve a consensus model of *S. coelicolor*,

441   yielding a comprehensive model useful for the scientific community.

Genome-scale models provide hypothesis for slow growth of M1152

443   The reduced growth rate of M1152 is correlated with reduced glucose uptake and enhanced

444   glutamate uptake compared to M145. This is expected to lead to a less active glycolysis but a

445   more active TCA cycle, and thus, a more active oxidative metabolism in M1152 compared to

446   M145. An active oxidative metabolism is known to generate oxidative stress, and indeed, the

447   *in vivo* data, as well as the genome-scale model, predict an increased oxidative stress in

448   M1152. The toxicity of oxidative stress might, at least in part, be responsible for the growth

449   delay of M1152, while the *rpoB* mutation may add to this phenotype, since one of the

450   functions of the ppGpp-associated RNA polymerase is to promote a growth arrest in

451   conditions of nutritional stress.

Further development may improve M1152 as host for heterologous expression

453   The strain M1152 has several advantages as a host for heterologous production of secondary

454   metabolites. The deletion of the 4 major BGCs not only removes presumed competing sinks

455   for valuable precursors, but also generates a clean background to ease the identification of

456   novel products by mass spectrometry. M1152 was already proven to be more efficient than

457   M145 and M1146 in heterologous production of the nitrogen-containing antibiotics

458   chloramphenicol and congocidine, as well as Act production from reintroduction of its BGC

459   (13). Strains M1146 and M1152 produce, respectively, 3- to 5-, and 20- to 40-fold more

460   chloramphenicol and congocidine from respective heterologous clusters than M145.

461   Furthermore, in strain M1317, derived from M1152 by additional removal of three Type III

462   PKS genes (16), the (re-)introduction of germicidin synthase gave a 10.7 and 7.8-fold increase

463   in the total germicidin production by M1317 and M1152, respectively. This demonstrated

464   that the *rpoB* mutation, earlier shown to have a positive impact on the biosynthesis of

465   secondary metabolites (13), has a higher impact on the production of these compounds than

466   the deletion of competing precursor sinks, even while it cannot be excluded that

467   unintended and unknown genetic differences introduced during strain development are

468   underlying some of the observed behaviours. Nonetheless, the comparative analysis of

469   M145 and M1152 provides valuable insight to the impact of the *rpoB* mutation on cellular

470   metabolism and its relationships with antibiotic production, while a dedicated, systematic

471   comparative analysis of M1152, M1146 (13) and M145 will be necessary to in detail dissect

472   the overlapping influences of BGC deletion and the *rpoB* mutation (99).

473   As earlier work has suggested a competition for common precursors (acetyl-CoA/malonyl-

474   CoA) between fatty acids and secondary metabolites biosynthesis (100), it could be

475   anticipated that the deletion of BGCs would have a positive effect on fatty acids, and thus

476   TAG biosynthesis, but our data indicate that this is not the case (**Figure 5**).

477

Materials and Methods

478

Sco-GEM consensus model reconstruction and development

479

480   A brief description of the model reconstruction process is given in the following section,

481   while all details are described in the **Supplemental Information.** and in the community

482   model's GitHub repository (https://github.com/SysBioChalmers/sco-GEM). The model is

483   hosted on GitHub to facilitate further development by the community, and we've also

484   created a channel on Gitter dedicated to Sco-GEM questions and discussions

485   (https://gitter.im/SysBioChalmers/Sco-GEM).

486   Protocol for model merging

487   Using iKS1317 (15) as a starting point, additional reactions, metabolites and genes were

488   added from Sco4 (37) and iAA1259 (35). These three models are all based on the preceding

489   model iMK1208. To facilitate model comparison, modified or added reactions and

490   metabolites in Sco4 and iAA1259 were mapped to the iKS1317 namespace by using reaction

491   and metabolite database annotations, reaction equations and metabolite names and

492   formulas. The full list of reactions and metabolites added or modified according to Sco4 and

493   iAA1259 is given in **Data Set S1, Tab 6 - 10.**

494   The next step of the reconstruction process involved mainly manual curations: known flaws

495   and missing gene annotations in iKS1317 and Sco4 were fixed; reactions and metabolites

496   added from Sco4 were given IDs according to the BiGG namespace (56); all reactions,

497   metabolites and genes were given SBO annotations (101) (**Data Set S1, Tab 11**); all possible

498   reactions and metabolites were given MetaNetX (55) and chebi (54) (metabolites only)

499   annotations; the extensive annotation of genes from iAA1259 were expanded to cover 1591

500   of the 1777 genes in Sco-GEM. We also created pseudo-metabolites for the redox cofactors

501   NADH/NADPH and NAD+/NADP+ and introduced them into reactions where the cofactor

502   usage is uncertain.

503   The biomass equation was curated with the following main improvements: 1) Adopting the

504   curation of 2-demethylmenaquinol and menaquinol from iAA1259; 2) Separating the

505   biomass reaction into the pseudometabolites lipid, protein, dna, rna, carbohydrate, cell wall

506   and misc; 3) Updating the coefficients for prosthetic groups based on the proteomics data

507 and information about prosthetic groups for individual proteins from UniProt. Additional

508 details are given in the **Supplemental Information**.

Model reversibility

510 By using python-API (https://gitlab.com/elad.noor/equilibrator-api) of eQuilibrator (59) we

511 calculated the change in Gibbs free energy for 770 reactions (**Data Set S1, Tab 3**).

512 eQuilibrator can only calculate the change in Gibbs free energy for intracellular reactions (i.e.

513 not transport and exchange reactions) where all metabolites are mapped to KEGG (51, 52).

514 The calculations are based on the component contribution method (102). The change in

515 Gibbs free energy was calculated at standard conditions (25 °C, 1 bar), pH7 and 1mM

516 concentration of reactants, denoted $\Delta_r G'^m$ in eQuilibrator. This did not cover any transport or

517 exchange reactions nor reactions with metabolites lacking KEGG annotation. We then

518 applied a threshold of -30 kJ/mol to define a reaction as irreversible (103, 104). Using the set

519 of growth data and knockout data, we evaluated the effect of these changes in reaction

520 reversibility: by randomly applying these changes to 10 reactions at the time, we identified

521 single, pair and triplets of reactions that reduced model accuracy when the reversibility was

522 changed based on the change in Gibbs free energy (**Data Set S1, Tab 12; Supplemental**

523 **Information**).

Analysis and annotation of transport reactions

525 Gene annotations, substrate and transport class information were mostly extracted from

526 Transport DB 2.0 (105) and TCDB (106). Then, transport proteins were extracted from

527 IUBMB-approved Transporter Classification (TC) System and categorized into 9 main classes

528 (**Figure 1F**): 1) ABC transporter; 2) PTS transporter; 3) Proton symporter; 4) Sodium

529 symporter; 5) Other symporter; 6) Proton antiport; 7) Other antiport; 8) Facilitated diffusion;

530   9) Simple diffusion. For those transport proteins with an ambiguous substrate annotation in

531   TCDB, the specific substrate annotation was obtain by extracting annotations from KEGG (51,

532   52), UniProt (57) or through BLAST homology search (107) using a similarity threshold of 90%

533   (**Supplemental Information; Data Set S1, Tab 4**).

534   Development of enzymatically constrained (EcSco-GEM) model

535   An enzyme-constrained version of the Sco-GEM model (denoted EcSco-GEM) was generated

536   using GECKO (31). The GECKO method enhances an existing GEM by explicitly constraining

537   the maximum flux through each reaction by the maximum capacity of the corresponding

538   enzyme, given by the product of the enzyme abundance and catalytic coefficient. This is

539   facilitated by splitting both, reactions catalysed by isoenzymes and reversible reactions. The

540   Sco-GEM v1.1 model was modified using GECKO version 1.3.4. Kinetic data, in the form of

541   k_{cat} values (s^{-1}), were automatically collected from BRENDA (108). If BRENDA did not report a

542   k_{cat} value for an enzyme, GECKO searched for alternative k_{cat} values by reducing specificity,

543   on the level of substrate, enzymatic activity (EC number) and organism. While 4178 out of

544   4753 queried enzyme activities could be matched to the full EC code, 306 of the matched

545   activities reported in BRENDA were from *S. coelicolor.* Additionally, six k_{cat} values were

546   manually curated, and a thorough explanation and reasoning behind these modifications are

547   given in the **Supplemental Information**. The NAD(H)/NAD(P)H pseudo-reactions were

548   blocked to avoid infeasible loops.

549   Then, separate models were created for each strain (the gene clusters for actinorhodin,

550   undecylprodigiosin, CDA and coelimycin P1 were removed to create M1152) and for each

551   time point by using estimated growth, uptake rates of glutamate and glucose, secretion

552   rates of undecylprodigiosin, germicidin A and B and proteome measurements (**Supplemental**

553   **Information**). These time point specific models (9 time points for M145, 8 time points for

554   M1152) were used to analyse the activity in individual metabolic pathways through random

555   sampling (65). We also created one EcSco-GEM model for each strain with a global

556   constraint on the protein usage instead of specific protein usage, which were used for model

557   quality control.

Continuous integration and quality control with memote

559   Validation and quality assessment of Sco-GEM is carried out using the test-suite in memote

560   (42). Memote provides by default a large range of tests, which we have used to identify

561   issues and possible improvements. The test suite reports descriptive model statistics such as

562   the number of genes, reactions and metabolites, and also checks the presence of SBO terms

563   and annotations, the charge and mass balance of all reactions, the network topology and

564   find energy-generating cycles (109). Additionally, we incorporated custom tests into the

565   memote test-suite to automatically compare predicted phenotypes with experimental data

566   in different growth media and for different knockout mutants. The experimental growth and

567   knockout data are extracted from (15). Memote version 0.9.12 was used in this work, and

568   the full memote report for Sco-GEM is given in the **Supplemental Information**. As a separate

569   evaluation, we applied the method for identifying internal and unrealistic energy-generating

570   cycles by (110) , and no such cycles were found in Sco-GEM.

571   The simplest use of memote is generating snapshot reports showing the current state of the

572   model. However, by integrating Travis CI [https://travis-ci.com/] into the gitHub repository,

573   memote can be used to create a continuous report displaying how each commit affects the

574   model quality.

Random sampling, normalization and pathway analysis

Because of the huge number of reactions in the EcSco-GEM, it is challenging to sample the solution space appropriately: we have chosen to use the method provided in the Raven Toolbox 2 (37, 65), which samples the vertices of the solution space. The drawback of this method is that it will not result in a uniform sampling of the solution space. However, it is more likely to span the entire solution space and also not prone to get stuck in extremely narrow parts of the solution space, which may happen with variants of the hit-and-run algorithm (111–113). For each of the time points for each strain (17 different conditions in total) we generated 5000 random flux distributions with Gurobi as the solver. The reactions catalysed by isoenzymes were combined into the set of reactions in Sco-GEM and the reactions providing protein for each reaction. The mean of the 5000 flux distributions for each metabolic reaction was used in the following analysis.

Finally, for each of the 17 conditions, the mean fluxes were normalized by the CO_2 production rate. Then, the normalized mean fluxes were summarized for each metabolic pathway by using the curated pathway annotations, and we consider this a measure of the metabolic activity in each pathway.

Since glucose and glutamate uptake rates, as well as growth rates were significantly different in the two strains and at different time points, normalization of the data was necessary to compare flux distributions. We tested various proxies as indicators of overall metabolic activity for normalization, namely CO_2 production; the total carbon uptake from glucose and glutamate; growth rate and mean flux value. As golden standard, we compared the fluxes through individual reactions that are well documented to change in M145 in response to the phosphate depletion (**Figure S8**). Normalization based on CO_2 production was tested and

598   gave similar results than the data normalized on total carbon uptake from glucose and

599   glutamate (**Figure S8A and S8B**. The data normalized by the sum of fluxes showed similar

600   patterns as those achieved by glucose/glutamate and CO_2-normalized data but was noisier

601   (**Figure S8C**). Considering the huge differences in growth rate, the growth-normalized data

602   masked any other flux patterns (**Figure S8D**). The fact that different normalizations provided

603   similar differences in metabolic fluxes proved that the inferred changes in metabolism were

604   not artefacts of the normalization method but represent true metabolic activity of each

605   strain.

606   Strains, cultivation conditions, sampling procedures, and analyses of media

607   components and antibiotics box

608   Experiments were performed using strain M145 of *S. coelicolor* A3(2) and its derivatives

609   M1146 and M1152. The latter two are lacking the 4 major BGCs for actinorhodin (Act),

610   undecylprodigiosin (Red), coelimycin P1 (Cpk), and calcium-dependent antibiotic (CDA),

611   while M1152 is also carrying the pleiotropic, previously described antibiotic production

612   enhancing mutation *rpoB* [S433L] (13, 22). All strains were kindly provided by Mervyn Bibb at

613   John-Innes-Centre, Norwich, UK.

614   Triplicate cultivations of the strains were performed based on germinated spore inoculum

615   on 1.8 L phosphate-limited medium SSBM-P, applying all routines of the optimized

616   submerged batch fermentation strategy for *S. coelicolor* established and described before

617   (20). All media were based on ion-free water, and all chemicals used were of analytical

618   grade. In brief, spore batches of M145, M1146 and M1152 were generated by cultivation on

619   soy flour-mannitol (SFM) agar plates (114), harvesting by scraping off spores and suspension

620   in 20% (v/v) glycerol, and storage in aliquots at −80 °C. 10^9 CFU of spores of each strain were

621 germinated for 5 hours at 30 °C and 250 rpm in 250 mL baffled shake-flasks with 2 g of 3 mm

622 glass beads and 50 mL 2x YT medium (115). The germinated spores were harvested by

623 centrifugation (3200 x g, 15 °C, 5 min) and re-suspended in 5 mL ion-free water. An even

624 dispersion of the germinated spores was achieved by vortex mixing (30 s), ensuring

625 comparable inocula among biological replicas. Each bioreactor (1.8 liter starting volume

626 culture medium in a 3-liter Applikon stirred tank reactor) was inoculated with 4.5 mL

627 germinated spore suspension (corresponding to 9×10^8 CFU). Phosphate-limited medium

628 SSBM-P (8) consisted of Na-glutamate, 55.2 g/L; D-glucose, 40 g/L; $MgSO_4$, 2.0 mM;

629 phosphate, 4.6 mM; supplemented minimal medium trace element solution SMM-TE (115),

630 8 mL/L and TMS1, 5.6 mL/L. TMS1 consisted of $FeSO_4$ x 7 H_2O, 5 g/L; $CuSO_4$ x 5 H_2O, 390

631 mg/L; $ZnSO_4$ x 7 H_2O, 440 mg/L; $MnSO_4$ x H_2O, 150 mg/L; Na_2MoO_4 x 2 H_2O, 10 mg/L; $CoCl_2$ x

632 6 H_2O, 20 mg/L, and HCl, 50 mL/L. Clerol FBA 622 fermentation defoamer (Diamond

633 Shamrock Scandinavia) was added to the growth medium before inoculation. Throughout

634 fermentations, pH 7.0 was maintained constant by automatic addition of 2 M HCl. Dissolved

635 oxygen levels were maintained at a minimum of 50% by automatic adjustment of the stirrer

636 speed (minimal agitation 325 rpm). The aeration rate was constant 0.5 L/(L x min) sterile air.

637 Dissolved oxygen, agitation speed and carbon dioxide evolution rate were measured and

638 logged on-line, while samples for the determination of cell dry weight, levels of growth

639 medium components and secondary metabolites concentrations, as well as for

640 transcriptome and proteome analysis were withdrawn throughout the fermentation trials as

641 indicated in **Figure 2B**. For transcriptome analysis, 3 × 4 ml culture sample were applied in

642 parallel onto three 0.45 μm nitrocellulose filters (Millipore) connected to vacuum. The

643 biomass on each filter was immediately washed twice with 4 ml double-autoclaved ion-free

644 water pre-heated to 30 °C, before the filters were collected in a 50 ml plastic tube, frozen in

645   liquid nitrogen and stored at -80 °C until RNA isolation. For proteome analysis, 5 ml samples

646   were taken and centrifuged (3200 x g, 5 min, 4 °C), and the resulting cell pellets frozen

647   rapidly at -80 °C until further processing.

648   Levels of phosphate were measured spectrophotometrically by using the SpectroQuant

649   Phosphate test kit (Merck KGaA, Darmstadt, Germany) following the manufacturer's

650   instructions after downscaling to 96-well plate format. D-glucose and L-glutamate

651   concentrations were determined by LC-MS using suitable standards, and measured

652   concentrations were used to estimate specific uptake and excretion rates.

653   Undecylprodigiosin (Red) levels were determined spectrophotometrically at 530 nm after

654   acidified methanol extraction from the mycelium (116). To determine relative amounts of

655   actinorhodins (determined as total blue pigments, TBP), cell culture samples were treated

656   with KOH (final concentration 1 M) and centrifuged, and the absorbance of the supernatants

657   at 640 nm was determined (116). Quantification of germicidin A and B was performed using

658   targeted LC-MS analytics.

659   Proteomics

660   Sample preparation and NanoUPLC-MS analysis

661   Quantitative proteomics were performed using pipeline previously described (117).

662   Mycelium pellets for proteome analysis were thawed and resuspended in the remaining

663   liquid. 50 μL re-suspended mycelium was withdrawn and pelleted by centrifugation. 100 μL

664   lysis buffer (4% SDS, 100 mM Tris-HCl pH 7.6, 50 mM EDTA) was added, and samples were

665   sonicated in a water bath sonicator (Biorupter Plus, Diagenode) for 5 cycles of 30 s high

666   power and 30 s off in ice water. Cell debris was pelleted and removed by centrifugation.

667   Total protein was precipitated using the chloroform-methanol method described before

668   (118). The pellet was dried in a vacuum centrifuge before dissolving in 0.1% RapiGest SF

669   surfactant (Waters) at 95 °C. The protein concentration was measured at this stage using

670   BCA method. Protein samples were then reduced by adding 5 mM DTT, followed by

671   alkylation using 21.6 mM iodoacetamide. Then trypsin (recombinant, proteomics grade,

672   Roche) was added at 0.1 μg per 10 μg protein. Samples were digested at 37 °C overnight.

673   After digestion, trifluoroacetic acid was added to 0.5% followed by incubation at 37 °C for 30

674   min and centrifugation to remove MS interfering part of RapiGest SF. Peptide solution

675   containing 8 μg peptide was then cleaned and desalted using STAGE-Tipping technique

676   (119). Final peptide concentration was adjusted to 40 ng/μL using sample solution (3%

677   acetonitrile, 0.5% formic acid) for analysis.

678   200 ng (5 μL) digested peptide was injected and analysed by reversed-phase liquid

679   chromatography on a nanoAcquity UPLC system (Waters) equipped with HSS-T3 C18 1.8 μm,

680   75 μm X 250 mm column (Waters). A gradient from 1% to 40% acetonitrile in 110 min

681   (ending with a brief regeneration step to 90% for 3 min) was applied. [Glu^1]-fibrinopeptide B

682   was used as lock mass compound and sampled every 30 s. Online MS/MS analysis was done

683   using Synapt G2-Si HDMS mass spectrometer (Waters) with an UDMS^E method set up as

684   described in (120).

685   Data processing and label-free quantification

686   Raw data from all samples were first analysed using the vender software ProteinLynx Global

687   SERVER (PLGS) version 3.0.3. Generally, mass spectrum data were generated using an MS^E

688   processing parameter with charge 2 lock mass 785.8426, and default energy thresholds. For

689   protein identification, default workflow parameters except an additional acetyl in N-terminal

690   variable modification were used. Reference protein database was downloaded from

691   GenBank with the accession number NC_003888.3. The resulted dataset was imported to

692   ISOQuant version 1.8 (120) for label-free quantification. Default high identification

693   parameters were used in the quantification process. TOP3 result was converted to PPM

694   (protein weight) and send to the modelers and others involved in interpreting the data (**Data**

695   **Set S1, Tab 13**).

696   TOP3 quantification was filtered to remove identifications meet these two criteria: 1.

697   identified in lower than 70% of samples of each strain and 2. sum of TOP3 value less than 1 ×

698   10^5. Cleaned quantification data was further subjected to DESeq2 package version 1.22.2

699   (29) and PCA was conducted after variance stabilizing transformation (vst) of normalized

700   data.

701   Transcriptomics

702   RNA extraction and quality control

703   Bacteria were lysed using RNAprotect Bacteria (Qiagen) and following the manufacturer´s

704   instruction. Briefly, filters containing bacteria were incubated with 4 ml of RNAprotect

705   Bacteria reagent. After centrifugation, resulting samples were lysed using 500 µl of TE buffer

706   (10 mM Tris·Cl, 1 mM EDTA, pH 8.0) containing 15 mg/ml lysozyme using 150-600 µm

707   diameter glass beads (Sigma) agitated at 30 Hz for 5 minutes in the TissueLyser II (Qiagen).

708   Total RNA was extracted using RNeasy mini kit (Qiagen) and 700 µl of the resulting lysate

709   complemented with 470 µl of absolute ethanol. RNAase-free DNase set (Qiagen) and

710   centrifugation steps were performed to prevent DNA and ethanol contamination. Elution

711   was performed using 30 µl of RNase-free water and by reloading the eluate on the column to

712   improve the RNA yield. The RNA concentration was measured using Qubit RNA BR Assay Kit

713   (ThermoFisher Scientific), RNA purity was assessed using A260/A280 and A260/A230 ratio

714   using the Nano Drop ND-1000 Spectrophotometer (PEQLAB). RNA Integrity Number was

715   estimated using RNA 6000 Nano Kit (Agilent) and the Bioanalyzer 2100 (Agilent).

Library preparation and sequencing

717   A total of 1 µg of total RNA was subjected to rRNA depletion using Ribo-Zero rRNA Removal

718   Kit Bacteria (Illumina). The cDNA libraries were constructed using the resulting tRNA and the

719   NEBNext Ultra II Directional RNA Library Prep Kit (NEB). Libraries were sequenced as single-

720   reads (75 bp read length) on an Illumina NextSeq500 platform at a depth of 8–10 million

721   reads each.

RNA-seq data assessment and analysis

723   Sequencing statistics including the quality per base and adapter content assessment of

724   resulting transcriptome sequencing data were conducted with FastQC v0.11.5 (121). All

725   reads mappings were performed against the reference strain of *Streptomyces coelicolor*

726   *A3(2)* (RefSeq ID NC_003888.3). The mappings of all samples were conducted with HISAT2

727   v2.1.0 (122). As parameters, spliced alignment of reads was disabled, and strand-specific

728   information was set to reverse complemented (HISAT2 parameter --no-spliced-alignment

729   and --rna-strandness "R"). The resulting mapping files in SAM format were converted to BAM

730   format using SAMtools v1.6 (123). Mapping statistics, including strand specificity estimation,

731   percentage of mapped reads and fraction exonic region coverage, were conducted with the

732   RNA-seq module of QualiMap2 v2.2.2-dev (124). Gene counts for all samples were

733   computed with featureCounts v1.6.0 (28) based on the annotation of the respective

734   reference genome, where the selected feature type was set to transcript records

735   (featureCounts parameter -t transcript).

736   Normalization and differential gene expression

737   Raw count files were imported into Mayday SeaSight (125) for common, time-series-wide

738   normalization. For this, the raw counts of all biological replicates of one strain across the

739   time-series were log2-transformed (with pseudocount of +1 for the genes with zero counts)

740   and then quantile-normalized. To make the two normalized time-series data of M154 and

741   M1152 comparable, they were again quantile-normalized against each other. The

742   normalized RNA-seq data are provided in **Data Set S1, Tab 14.**

743   Differentially expressed genes were identified by ANOVA using Orange (v3.2) and the

744   bioinformatic toolkit (v), with FDR of <0.01 and a minimal fold enrichment >1 for at least one

745   aligned time point. Genes with low expression (log2 < 5 for both strains and time points)

746   were not considered for further analysis. The differentially expressed genes were

747   subsequently scaled to the expression average and clustered by K-means. Visualization of

748   genes and clusters were performed in python (v3.7) with matplotlib (v3.1.1). For this, the

749   time-series of M145 and M1152 were aligned such that in the visual representation, the

750   expression profiles of the two strains are aligned relative to the time point of phosphate

751   depletion. Both DAVID (126, 127) and the string database (128) was used to evaluate the

752   function of each cluster, identifying overrepresentation of function groups based on GO

753   annotation or text mining. Identified differential clusters or regulons were extracted from

754   literature and plotted (**Data Set S1, Tab 5; Figure S7**).

755

Data and Software Availability

Model repository

The model is hosted and developed in an open repository on GitHub:

https://github.com/SysBioChalmers/Sco-GEM. Here, the latest version of the Sco-GEM is

available in both YAML and SBML level 3 Version 1. Additionally, users can see all details of

the model reconstruction and contribute to further model development by posting issues or

suggest changes. This should encourage further, incremental development of Sco-GEM by

the community.

Proteome data

The proteomics data have been deposited to the ProteomeXchange Consortium via the

PRIDE (129) partner repository with the dataset identifier PXD013178 and

10.6019/PXD013178. Normalized proteome data is also available in **Data Set S1, Tab 13.**

Transcriptomics data

All high-throughput sequencing data have been deposited in NCBI's Gene Expression

Omnibus and are accessible under accession number GSE132487 (M145) and GSE132488

(M1152). Normalized counts are also found in **Data Set S1, Tab 14.**

Author contributions

Conceptualization, E.K., E.A., A.W., S.S., A.S.Y. and T.K. Methodology and software, E.K., S.S.,

A.S.Y. and T.K. Validation and formal analysis, C.D., K.N., D.V.D., S.S., T.K., E.K. Investigation,

T.K., A.W., S.S., E.K. Data curation, S.S., T.K. Writing - original draft, S.S., T.K., D.V.D., C.D.,

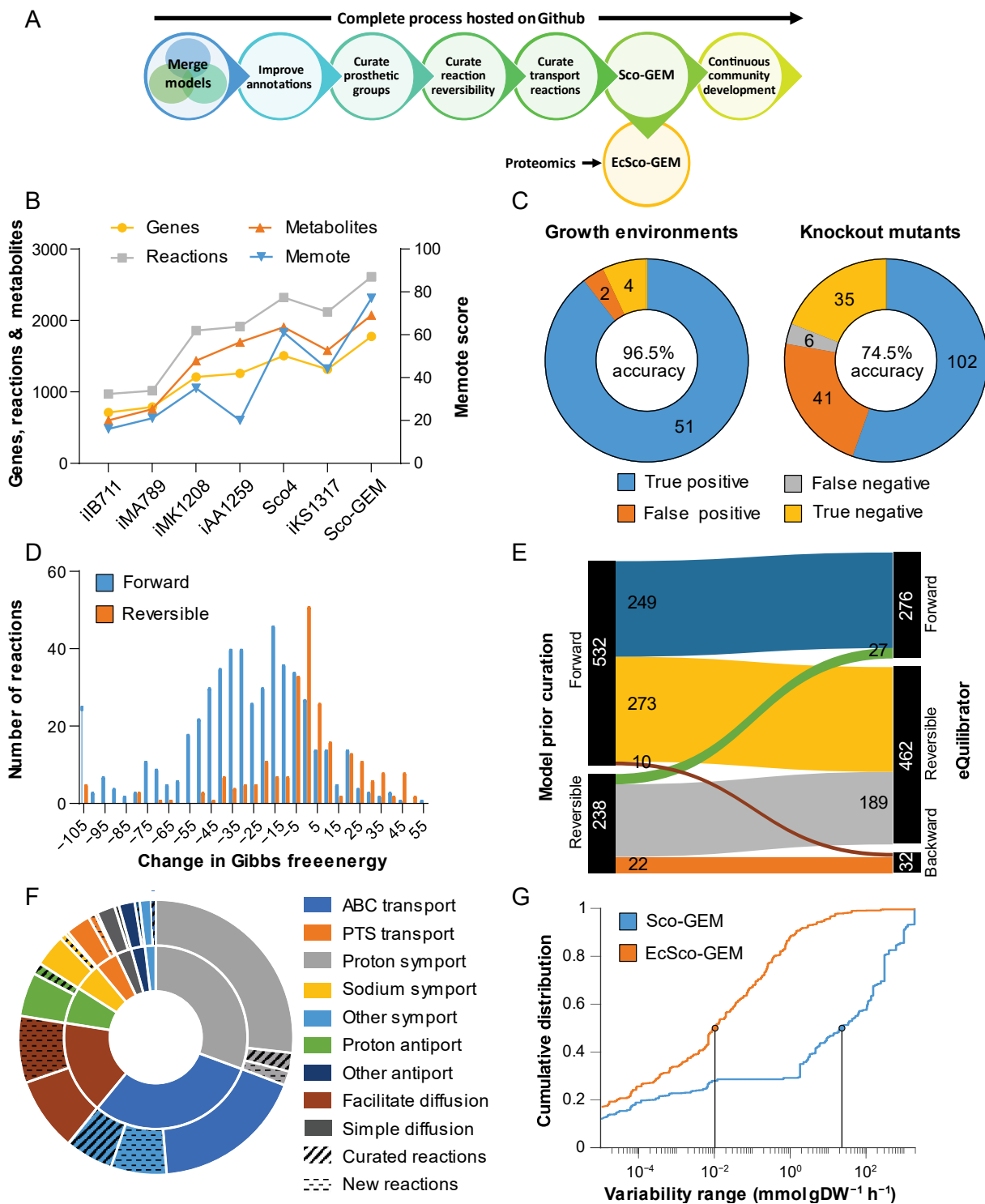K.N. Writing – review & editing, all authors. Visualization, S.S., E.K., C.D., D.V.D. Supervision,

A.W., E.A., E.K., G.W. Project administration, A.W. Funding acquisition: A.W., E.K., E.A., G.W.

## Acknowledgements

791   Figures

792

793   **Figure 1: Sco-GEM development and analysis.** A) Schematic overview of the various steps in

794   the Sco-GEM reconstruction process. B) The overall memote score and number of genes,

795   reactions and metabolites for the 7 published *S. coelicolor* GEMs. C) Assessment of the model

796   quality by comparing *in vivo* observations with *in silico* predictions. D) The change in Gibbs

797   free energy for 770 reactions that were annotated as either reversible or forward irreversible

798   in the model prior curation of reaction reversibility. The histogram is truncated at -105 kJ/mol,

799   and more negative values are assigned to the leftmost bin. E) Analysis and comparison of the

800   directionality and reversibility of reactions prior curation and the direction inferred from the

801   change in Gibbs free energy as estimated by eQuilibrator. F) Overview of the 369 transport

802   reactions included in Sco-GEM, whereof 42 were curated and 65 added during this work. The

803   inner ring categorizes the reactions into 9 different subgroups, while the outer ring displays

804   the amount of curated and added reactions within each category. G) Comparison of

805   cumulative flux variability distributions, demonstrating that the incorporation of kinetic

806   coefficients in EcSco-GEM greatly constrains the solution space.
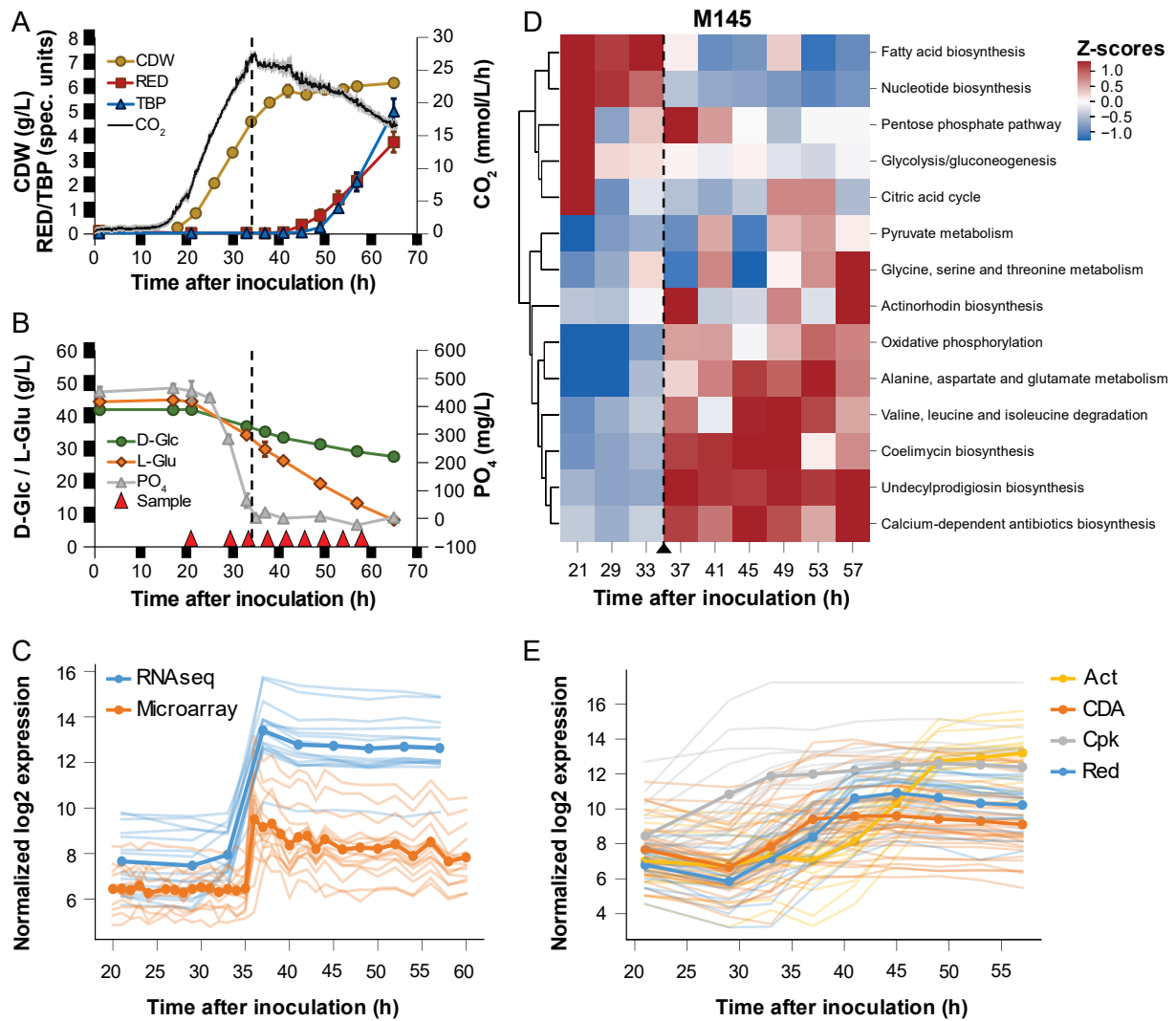
Figure 2: Batch cultivation of *S. coelicolor* M145 and the effect of phosphate depletion.

Compounds produced (A) and consumed (B) during batch fermentation of *S. coelicolor* M145. Time points for sampling for transcriptome and proteome analysis are indicated with red triangles. The dashed vertical line indicates when phosphate in the medium has been depleted. Error bars are standard deviations of three biological replicates. CDW, Cell Dry Weight; Red, undecylprodigiosin; TBP, Total Blue Pigments/actinorhodins; CO_2 volume corrected respiration; D-Glc, D-glucose; L-Glu, L-glutamate; PO_4, phosphate. C) Comparison of previously published microarray data (8) and RNA-seq data (this study) for genes previously found to respond to phosphate depletion (8). D) Clustered heatmap of CO_2-normalized Z-scores for each of the top 10 varying pathways plus the pathways for the 4 major BGCs in

818   M145, as revealed by simulations with the proteomics-integrated EcSco-GEM model. The

819   dashed vertical line indicates the time point of the metabolic switch. E) RNA-seq data of the 4

820   major BGCs show the onset of biosynthesis of actinorhodin (Act), calcium-dependent

821   antibiotic (CDA), coelimycin P1 (Cpk) and undecylprodigiosin (Red) at different time points

822   during the batch fermentations of M145.
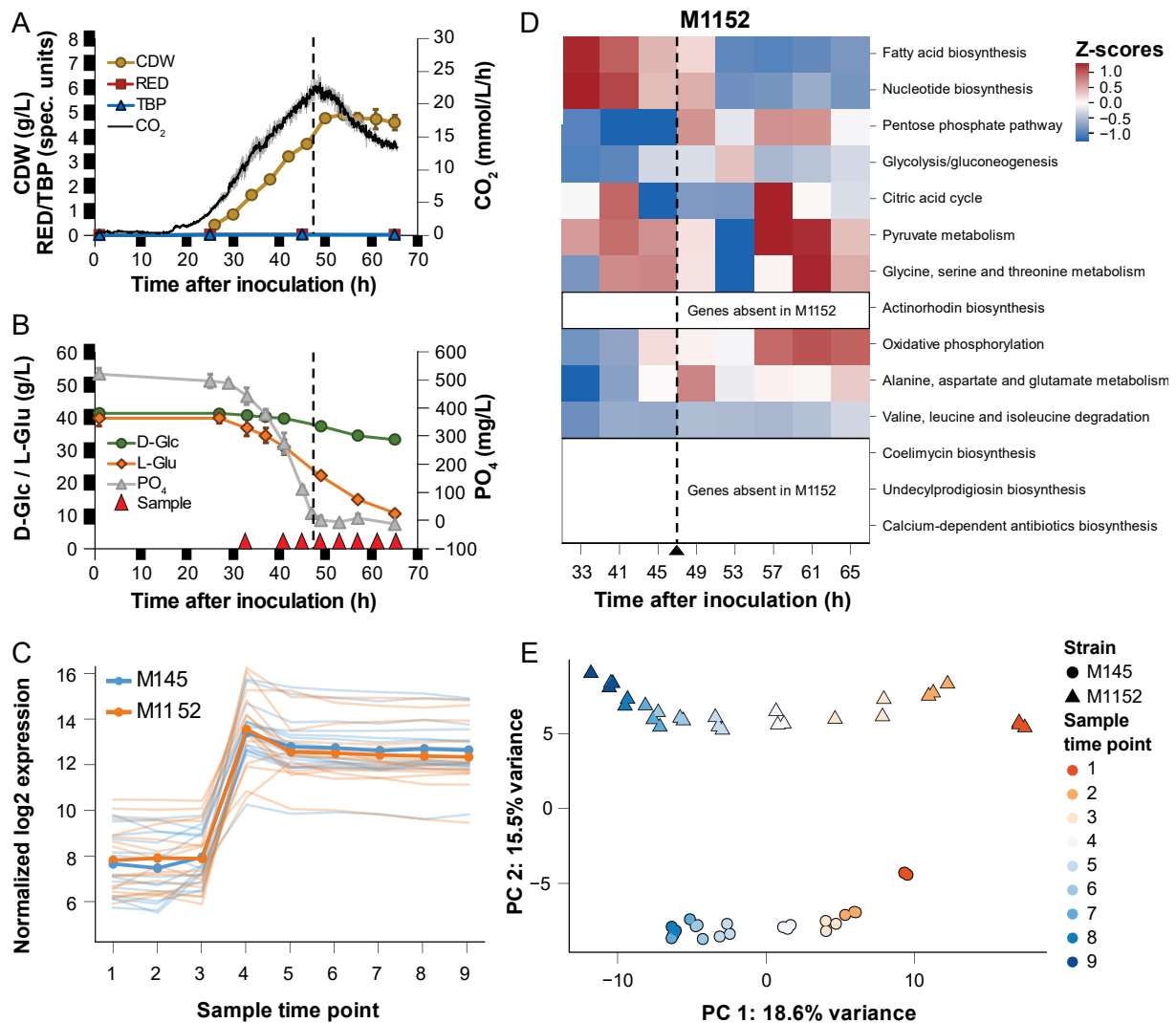
824   **Figure 3: Batch cultivation of *S. coelicolor* M1152.** Compounds produced (A) and consumed

825   (B) during batch fermentation of *S. coelicolor* M1152. Time points for sampling for

826   transcriptome and proteome analysis are indicated with red triangles. The dashed vertical line

827   indicates when phosphate in the medium has been depleted. Error bars are standard

828   deviations of three biological replicates. CDW, Cell Dry Weight; Red, undecylprodigiosin; TBP,

829   Total Blue Pigments/actinorhodins; CO_2, volume corrected respiration; D-Glc, D-glucose; L-

830   Glu, L-glutamate; PO_4, phosphate. C) Alignment of sample time points of M145 and M1152

831   cultivations based on the expression profiles of genes that were earlier found to respond to

832   phosphate depletion in respect to the metabolic switch (8). D) Clustered heatmap of

833   proteomics data for M145 (triangles) and M1152 (circles), for each time-point and culture.

834   The first principal component separates the time points, while the second principal

835   component separates the two strains. E) CO_2-normalized Z-scores of pathway fluxes predicted

836   by EcSco-GEM for 10 of the most varying pathways in M145 and M1152. The data for M145

837   (**Figure 2D**) and M1152 are standardized together to make values and colours comparable. E)

838   Principle component analysis of the proteomics data for M145 (triangles) and M1152 (circles),

839   for each time-point and culture. The first principal component separates the time points while

840   the second principal component separates the two strains.
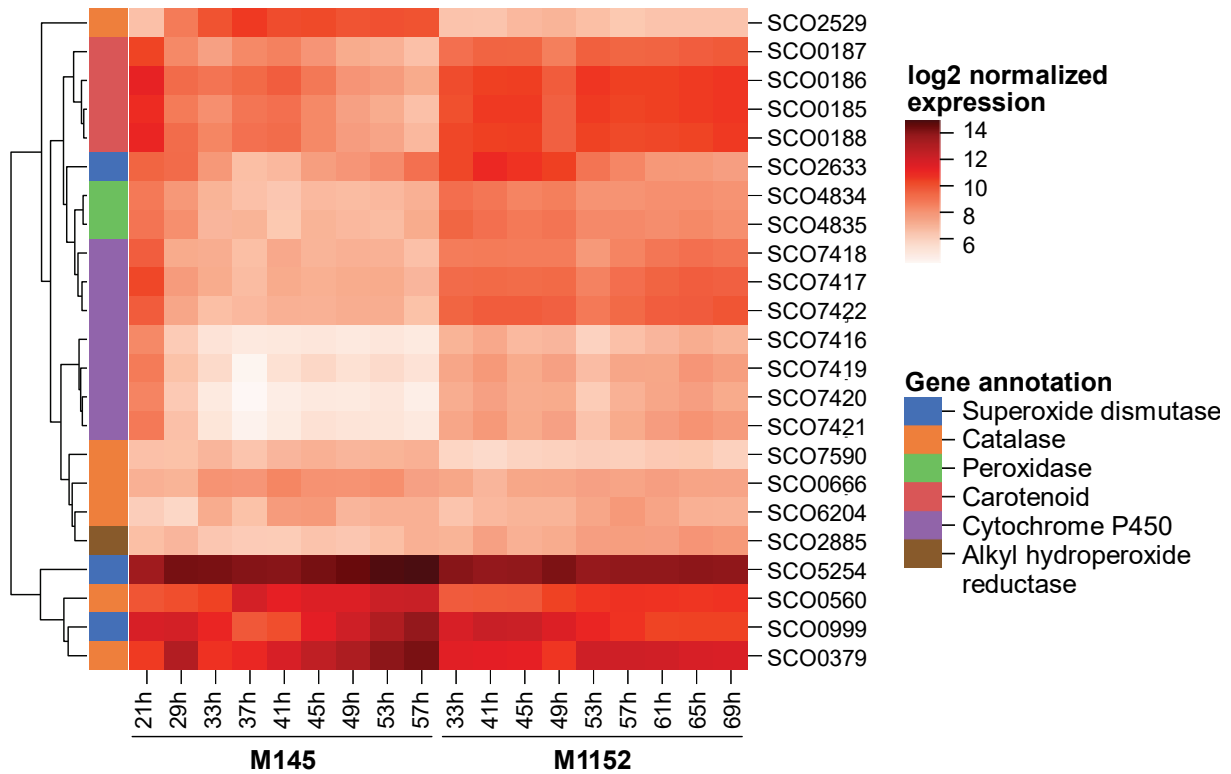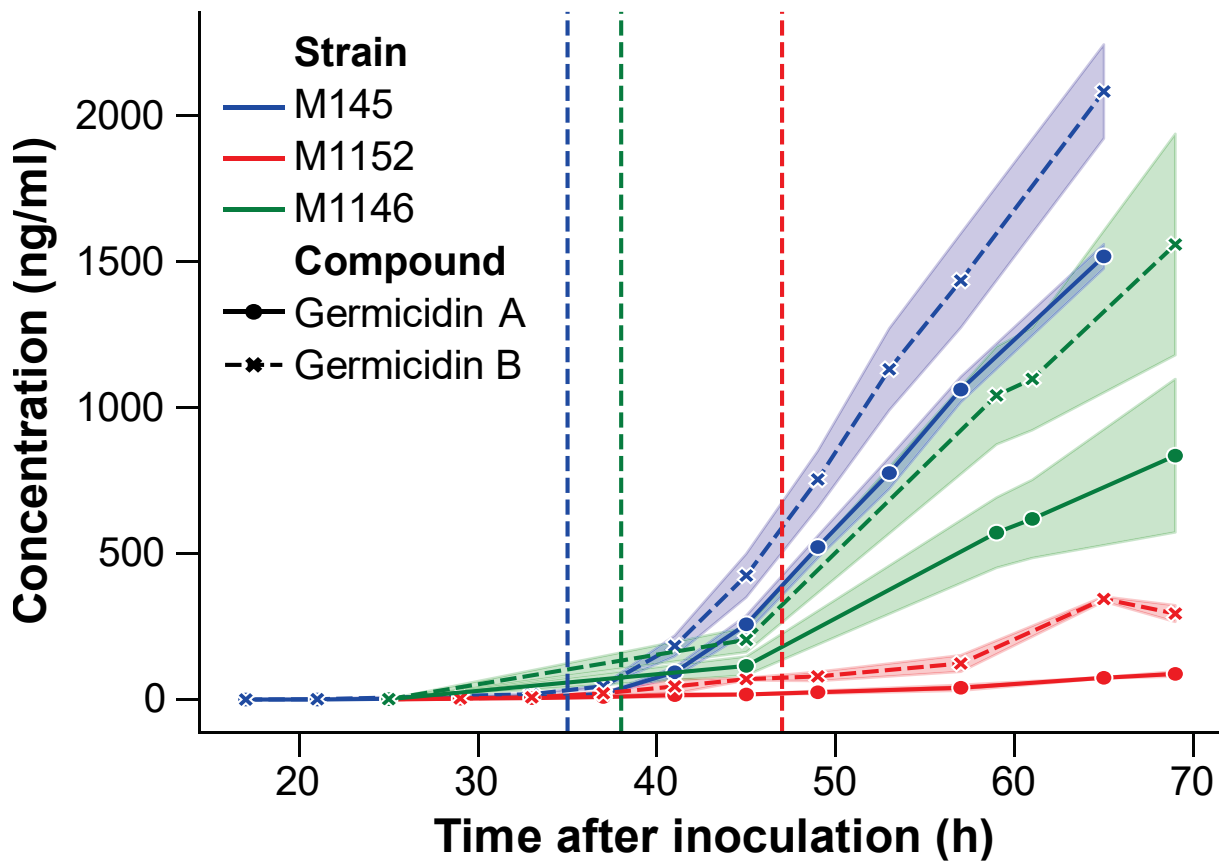
841
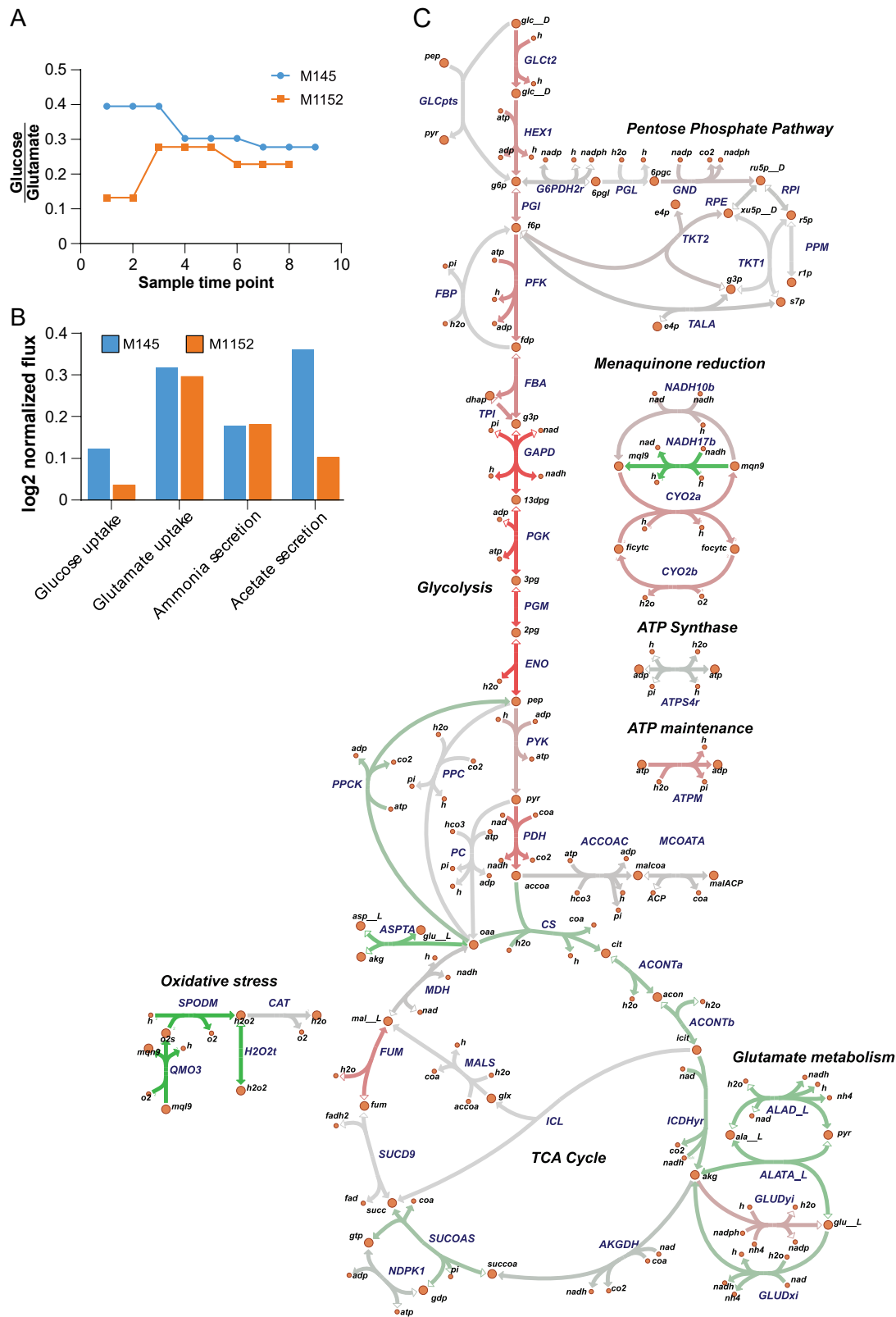
Figure 4: Predicted carbon fluxes in M145 and M1152. A) The ratio between estimated uptake

rates of glucose and glutamate showing that M1152 acquires a smaller part of its carbon from

glucose compared to M145. B) Roughly half of the nitrogen from glutamate is excreted as

845 ammonium (both strains), while higher uptake of glucose in M145 leads to more excretion of

846 acetate. C) Comparison of predicted fluxes for the second sampling time points for M145 and

847 M1152, i.e. after 29 and 41 hours, respectively. The second time point for each strain was

848 chosen because the estimated uptake rates are more reliable than the first time point. The

849 strength of the colour of the lines correspond to the flux difference between the strains; green

850 reactions have higher flux in M1152, and red reactions have higher flux in M145. Note the

851 reduced biomass-specific uptake rate of glucose and increased oxidative stress in M1152.

852
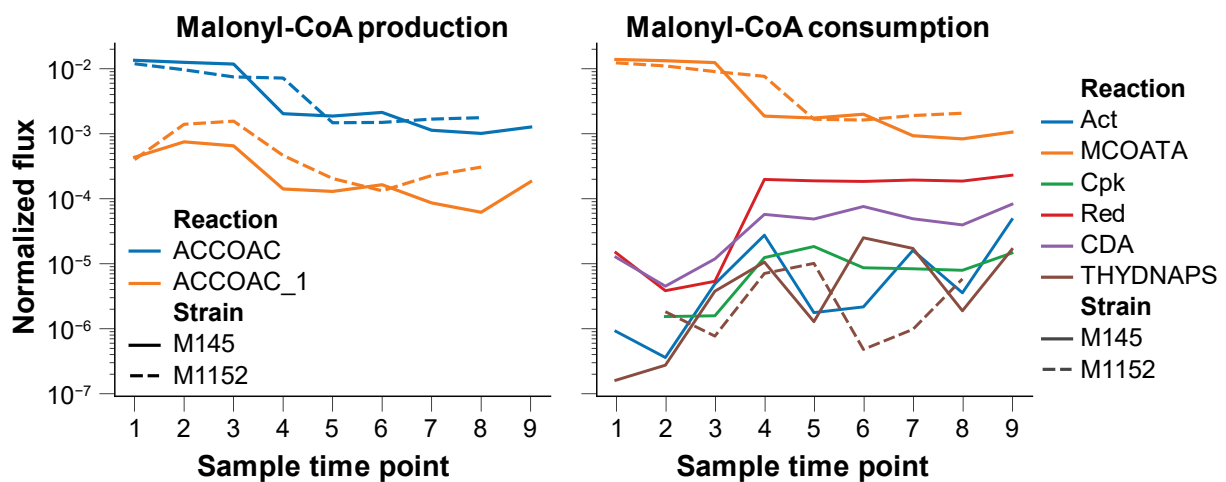
853 **Figure 5: Production and consumption of malonyl-CoA as the branching point between fatty**

854 **acid biosynthesis and production of polyketides**. From EcSco-GEM predictions, a reduced

855 malonyl-CoA production (left panel) by both acetyl-CoA carboxylase (ACCOAT; blue) and

856 acetyl-CoA carboxytransferase (ACCOAT_1; orange) is observed in both strains. Most of the

857 malonyl-CoA is consumed by fatty acid biosynthesis through malonyl-CoA-ACP transacylase

858 (MCOATA), even after metabolic switching, and this consumption balances the malonyl-CoA

859 production. The other main sinks for malonylmalonyl-CoA are the pathways encoded by the 4

860 major BGCs (Act, Cpk, Red and CDA) in addition to biflaviolin synthase (THYDNAPS).

Figure 6: Heatmap displaying log-transformed RNA-seq data of genes associated with oxidative stress. Included are genes related to oxidative stress either present in Sco-GEM or within the 499 differentially expressed genes. A general upregulation in M1152 and the first time point of M145 is observed.

Figure 7: Concentrations of germicidin A and B produced by M145, M1146 and M1152. The shaded regions display the uncertainty range (± 1 standard deviation) based on three replicate cultivations. Germicidin production rates after the metabolic switch (in ng ml^{-1} hour^{-1}) are: 41.4 (A) and 75.5 (B) for M145; 30.2 (A) and 56.4 (B) for M1146; 3.3 (A) and 13.3 (B) for M1152. Note that the growth rate is different between the strains, displayed by the vertical lines representing phosphate depletion at 35, 38 and 47 hours for M145, M1146 and M1152, respectively.

Supplemental Figures

Figure S1: Reaction subsystems and origin. The number of reactions in Sco-GEM in each of the 15 subsystems, and from which model they originate from. The other reactions (orange) are added during reconstruction of Sco-GEM.

878 **Figure S2: Gene clusters associated with metabolic switch.** RNA-seq (left column) and

879 proteomics (right column) from M145 of the 8 gene clusters associated with the metabolic

880 switch as previously identified (8). The 8 clusters are: A) genes related to ribosomal proteins;

881 B) genes related to nitrogen metabolism; C) Cpk gene cluster; D) genes related to

882 development; E) genes upregulated in response to phosphate depletion; F) genes involved in

883 synthesis of phosphate-free polymers; G) Act gene cluster; H) Red gene cluster

884 **Figure S3: Log-transformed expression levels of genes related to nitrogen metabolism.** The

885 glutamate import (SCO5774-5777), the glutamate sensing system *gluR-gluK* (SCO5778 and

886 SCO57779), *glnR* (SCO4159) and *glnA* (SCO2198) are downregulated subsequent to phosphate

887 depletion. We also observe that the first time point in M145 is very different from all other

888 samples.

889 **Figure S4: Clustered heatmaps of Z-score based on CO_2-normalized sum of fluxes of all**

890 **pathways standardized within each pathway and separated into different subsystems /**

891 **parts of the metabolism.** A) Central carbon metabolism. B) Amino acid metabolism. C)

892 Metabolism of vitamins and cofactors. D) Pathways of Biosynthetic gene clusters. E) Lipid

893 metabolism. F) Oxidative stress. G) Degradation of toxic compounds. H) All other pathways.

894 For all panels only pathway with a minimum flux of 1e-8 mmol $(g DW)^{-1} h^{-1}$ were included.

895 **Figure S5**: **RNA-seq, proteome and flux prediction of specific gene clusters and reactions.** A)

896 EcSco-GEM predicts that the flux through citrate synthase (CS) and isocitrate dehydrogenase

897 (ICDHyr) increases at later time points in M145, effectively increasing the shuttling of acetyl-

898 CoA into the TCA cycle. B) Log2 normalized expression data of genes involved in oxidative

899 phosphorylation indicate an increasing expression at later time points, while overall

900 expression in M1152 is higher than in M145. C-H) Comparison of log2 normalized expression

901   data as calculated with (log2 M145)-log2(M1152), where positive values indicate upregulation

902   in M145 relative to M1152, and vice versa for negative values. C) Increased expression of

903   genes of the afsR regulon in M145, while no significant difference in expression is observed

904   for (D) scbR regulon; (E) adpA regulon; (F) argR regulon; (G) genes induced by ppGPP; and (H)

905   genes repressed by ppGpp.

906   **Figure S6: Analysis of transcriptome data of genes.** A) Unsupervised clustering (k-means) of

907   significantly changed genes into 7 clusters: the first three (clusters 1-3) are upregulated in

908   M1152, while the last four (clusters 4-7) are upregulated from the beginning or at later time

909   points in M145. B-D) Comparison of log2 normalized expression data as calculated with (log2

910   M145)-log2(M1152), where positive values indicate upregulation in M145 relative to M1152,

911   and vice versa for negative values. B) Genes in the SoxR regulon are reducing expression in

912   M1152 at later time points. C) Almost all genes in the ATP-synthase cluster are up-regulated

913   in M1152 after the first time point. D) Also, the transcription of ribosomal protein genes after

914   the metabolic switch is increased in M1152 compared to M145. E) Batch cultivation of *S.*

915   *coelicolor* M1146. Error bars are standard deviations of three biological replicates. CDW, Cell

916   Dry Weight; CO_2 volume corrected respiration; PO_4, phosphate.

917   **Figure S7: Gene Ontology enrichment analysis of the 7 clusters identified in the 499**

918   **differentially expressed genes, categorized by function into four clustered heatmaps.**

919   Each heatmap shows the p-value for the enrichment of each GO-process. A) Genes related to

920   reactive oxygen species, the ribosome or development process and cell wall formation. B)

921   Oxireductase and iron / metal ion homeostasis. C) Regulation, biosynthesis and metabolism

922   related to RNA and DNA. D) All other GO-annotations. E) This color palette is the legend for

923   the column colors on top of each heatmap which displays which of the seven clusters each

924 gene belongs to. The red palette covers cluster 1-3 (upregulated in M1152), while the blue

925 palette covers cluster 4-7 (upregulated in M145). Note that no GO-processes were enriched

926 for the genes in cluster 2.

927 **Figure S8: Comparison of normalization methods of randomly sampled fluxes**. Heatmap

928 showing mean flux values normalized by A) total carbon uptake from glucose and glutamate,

929 B) CO_2 production, C) sum of all fluxes and D) growth rate. Because the mean flux values in

930 these reactions are different by several orders of magnitude, we display the data as

931 standardized values (for each reaction).

932

933 Other Supplemental material

934 **Supplemental Information:** The Memote report of Sco-GEM, the protocols for Sco-GEM and

935 EcSco-GEM development and a detailed description of estimation of rates from batch

936 fermentation data.

937 **Data Set S1**

938 **Tab 1:** Detailed overview of the script performing the reconstruction of Sco-GEM.

939 **Tab 2:** Comparison of the new biomass reaction in Sco-GEM with the biomass reaction in

940 iAA1259.

941 **Tab 3:** Reversibility prior update, calculated change in Gibbs free energy and standard

942 deviation of the calculated change in Gibbs free energy of 770 reactions in Sco-GEM.

943 **Tab 4:** Overview of all transport reactions added or curated during the process of Sco-GEM

944 model development, and the metabolites added along with the new transport reactions.

945   **Tab 5:** Genes present in the 7 clusters identified with K-Means clustering of the

946   differentially expressed genes.

947   **Tab 6:** Sco4 ID, name and Sco-GEM ID of the reactions added from Sco4 to Sco-GEM.

948   **Tab 7:** Sco4 ID, name and Sco-GEM ID of the metabolites added from Sco4 to Sco-GEM

949   **Tab 8:** Reaction ID, name and gene annotation of reactions added from iAA1259 to Sco-

950   GEM.

951   **Tab 9:** List of reactions modified according to iAA1259.

952   **Tab 10**: Metabolite ID and name of metabolites added from Sco4 to Sco-GEM.

953   **Tab 11**: List of SBO terms used in Sco-GEM

954   **Tab 12**: Single, pair and triplets of reactions which reduced model accuracy, in total 56

955   different reactions. The reversibility of these reactions was not changed according to the

956   predicted change in Gibbs free energy.

957   **Tab 13**: Normalized proteome data for M145 and M1152.

958   **Tab 14**: Normalized RNA-seq data for all six fermenters. M145 is cultivated in F516-F518,

959   while M1152 is cultivated in F519, F521, F522. Re-index IDs corresponds to sampling time

960   point (1-9) and strain.

961   **Tab 15**: List of genes within each cluster known to be associated with the metabolic switch.

962

963

References

1. Hopwood, David A. 2007. Streptomyces in nature and medicine: the antibiotic makers. Oxford University Press, USA.

2. Hahn J-S, Oh S-Y, Roe J-H. 2002. Role of OxyR as a Peroxide-Sensing Positive Regulator in Streptomyces coelicolor A3(2). Journal of Bacteriology 184:5214–5222.

3. Hutchings MI, Hoskisson PA, Chandra G, Buttner MJ. 2004. Sensing and responding to diverse extracellular signals? Analysis of the sensor kinases and response regulators of Streptomyces coelicolor A3(2). Microbiology, 150:2795–2806.

4. Nothaft H, Rigali S, Boomsma B, Swiatek M, McDowall KJ, van Wezel GP, Titgemeyer F. 2010. The permease gene nagE2 is the key to N-acetylglucosamine sensing and utilization in Streptomyces coelicolor and is subject to multi-level control. Molecular Microbiology 75:1133–1144.

5. Rigali S, Titgemeyer F, Barends S, Mulder S, Thomae AW, Hopwood DA, van Wezel GP. 2008. Feast or famine: the global regulator DasR links nutrient stress to antibiotic production by Streptomyces. EMBO reports 9:670–675.

6. Sola-Landa A, Rodríguez-García A, Franco-Domínguez E, Martín JF. 2005. Binding of PhoP to promoters of phosphate-regulated genes in Streptomyces coelicolor: identification of PHO boxes. Molecular Microbiology 56:1373–1385.

7. Chandra G, Chater KF. 2014. Developmental biology of Streptomyces from the perspective of 100 actinobacterial genome sequences. FEMS Microbiol Rev 38:345–379.

985   8.   Nieselt K, Battke F, Herbig A, Bruheim P, Wentzel A, Jakobsen ØM, Sletta H, Alam MT,

986   Merlo ME, Moore J, Omara WA, Morrissey ER, Juarez-Hermosillo MA, Rodríguez-García

987   A, Nentwich M, Thomas L, Iqbal M, Legaie R, Gaze WH, Challis GL, Jansen RC, Dijkhuizen

988   L, Rand DA, Wild DL, Bonin M, Reuther J, Wohlleben W, Smith MC, Burroughs NJ, Martín

989   JF, Hodgson DA, Takano E, Breitling R, Ellingsen TE, Wellington EM, Kolter R, Siegele D,

990   Tormo A, Hesketh A, Bucca G, Laing E, Flett F, Hotchkiss G, Smith C, Chater K, Hesketh

991   A, Chen W, Ryding J, Chang S, Bibb M, Huang J, Lih C, Pan K, Cohen S, Lian W, Jayapal K,

992   Charaniya S, Mehra S, Glod F, Kyung Y, Sherman D, Hu W, Strauch E, Takano E, Baylis H,

993   Bibb M, DeRisi J, Iyer V, Brown P, Reuther J, Wohlleben W, Fink D, Weissschuh N,

994   Reuther J, Wohlleben W, Engels A, Tiffert Y, Supra P, Wurm R, Wohlleben W, Wagner R,

995   Reuther J, Pawlik K, Kotowska M, Chater K, Kuczek K, Takano E, Takano E, Chakraburtty

996   R, Nihira T, Yamada Y, Bibb M, Takano E, Kinoshita H, Mersinias V, Bucca G, Hotchkiss

997   G, Nihira T, Smith C, Bibb M, Wohlleben W, Chater K, Kotowska M, Pawlik K, Smulczyk-

998   Krawczyszyn A, Bartosz-Bechowski H, Kuczek K, Claessen D, Rink R, Jong W de, Siebring

999   J, Vreugd P de, Boersma F, Dijkhuizen L, Wosten H, Bibb M, Molle V, Buttner M, Ryding

1000   N, Kelemen G, Whatling C, Flardh K, Buttner M, Chater K, Ohnishi Y, Seo J, Horinouchi

1001   S, Sola-Landa A, Moura R, Martín J, Sola-Landa A, Rodríguez-García A, Franco-

1002   Domínguez E, Martín J, Rodríguez-García A, Barreiro C, Santos-Beneit F, Sola-Landa A,

1003   Martín J, Sola-Landa A, Rodríguez-García A, Apel A, Martín J, Feitelson J, Malpartida F,

1004   Hopwood D, Hallam S, Malpartida F, Hopwood D, Takano E, Gramajo H, Strauch E,

1005   Andres N, White J, Bibb M, Kieser T, Bibb M, Buttner M, Chater K, Hopwood D, Bystrykh

1006   L, Fernandez-Moreno M, Herrema J, Malpartida F, Hopwood D, Dijkhuizen L, Irizarry R,

1007   Bolstad B, Collin F, Cope L, Hobbs B, Speed T, Ihaka R, Gentleman R, Dietzsch J,

1008   Gehlenborg N, Nieselt K. 2010. The dynamic architecture of the metabolic switch in

1009   Streptomyces coelicolor. BMC Genomics 11:10.

1010   9.   Thomas L, Hodgson DA, Wentzel A, Nieselt K, Ellingsen TE, Moore J, Morrissey ER, Legaie

1011   R, STREAM Consortium TS, Wohlleben W, Rodríguez-García A, Martín JF, Burroughs NJ,

1012   Wellington EMH, Smith MCM. 2012. Metabolic switches and adaptations deduced from

1013   the proteomes of Streptomyces coelicolor wild type and phoP mutant grown in batch

1014   culture. Molecular & cellular proteomics : MCP 11:M111.013797.

1015   10.   Bentley SD, Chater KF, Cerdeño-Tárraga A-MA-M, Challis GL, Thomson NR, James KD,

1016   Harris DE, Quail MA, Kieser H, Harper D, Bateman A, Brown S, Chandra G, Chen CW,

1017   Collins M, Cronin A, Fraser A, Goble A, Hidalgo J, Hornsby T, Howarth S, Huang C-HC-H,

1018   Kieser T, Larke L, Murphy L, Oliver K, O'Neil S, Rabbinowitsch E, Rajandream MM-A,

1019   Rutherford K, Rutter S, Seeger K, Saunders D, Sharp S, Squares R, Squares S, Taylor K,

1020   Warren T, Wietzorrek A, Woodward J, Barrell BG, Parkhill J, Hopwood DA. 2002.

1021   Complete genome sequence of the model actinomycete Streptomyces coelicolor A3(2).

1022   Nature 417:141–147.

1023   11.   Gomez-Escribano JP, Song L, Fox DJ, Yeo V, Bibb MJ, Challis GL. 2012. Structure and

1024   biosynthesis of the unusual polyketide alkaloid coelimycin P1, a metabolic product of

1025   the cpk gene cluster of Streptomyces coelicolor M145. Chem Sci 3:2716–2720.

1026   12.   Castro JF, Razmilic V, Gomez-Escribano JP, Andrews B, Asenjo JA, Bibb MJ. 2015.

1027   Identification and Heterologous Expression of the Chaxamycin Biosynthesis Gene

1028   Cluster from Streptomyces leeuwenhoekii. Appl Environ Microbiol 81:5820–5831.

1029   13.   Gomez-Escribano JP, Bibb MJ. 2011. Engineering Streptomyces coelicolor for

1030   heterologous expression of secondary metabolite gene clusters. Microbial

1031   Biotechnology 4:207–215.

1032   14.   Gomez-Escribano JP, Bibb MJ. 2014. Heterologous expression of natural product

1033   biosynthetic gene clusters in Streptomyces coelicolor: from genome mining to

1034   manipulation of biosynthetic pathways. Journal of Industrial Microbiology &

1035   Biotechnology 41:425–431.

1036   15.   Kumelj T, Sulheim S, Wentzel A, Almaas E. 2018. Predicting Strain Engineering Strategies

1037   Using iKS1317: A Genome-Scale Metabolic Model of Streptomyces coelicolor.

1038   Biotechnology Journal 0:1800180.

1039   16.   Thanapipatsiri A, Claesen J, Gomez-Escribano J-P, Bibb M, Thamchaipenet A. 2015. A

1040   Streptomyces coelicolor host for the heterologous expression of Type III polyketide

1041   synthase genes. Microb Cell Fact 14.

1042   17.   Yin J, Hoffmann M, Bian X, Tu Q, Yan F, Xia L, Ding X, Francis Stewart A, Müller R, Fu J,

1043   Zhang Y. 2015. Direct cloning and heterologous expression of the salinomycin

1044   biosynthetic gene cluster from Streptomyces albus DSM41398 in Streptomyces

1045   coelicolor A3(2). Scientific Reports 5:15081.

1046   18.   Nepal KK, Wang G. 2019. Streptomycetes: Surrogate hosts for the genetic manipulation

1047   of biosynthetic gene clusters and production of natural products. Biotechnology

1048   Advances 37:1–20.

1049   19.   Rutledge PJ, Challis GL. 2015. Discovery of microbial natural products by activation of

1050   silent biosynthetic gene clusters. Nature Reviews Microbiology 13:509–523.

1051   20.   Wentzel A, Bruheim P, Øverby A, Jakobsen ØM, Sletta H, Omara WAM, Hodgson DA,

1052   Ellingsen TE, Hopwood D, Bentley S, Chater K, Cerdeno-Tarraga A, Challis G, Thomson

1053   N, James K, Harris D, Quail M, Kieser H, Harper D, Klieneberger-Nobel E, Chater K,

1054   Hopwood D, Chater K, Bibb M, Lakey J, Lea E, Rudd B, Wright H, Hopwood D, Wright L,

1055   Hopwood D, Feitelson J, Hopwood D, Bibb M, Rokem J, Lantz S, Eliasson A, Nielsen J,

1056   Song S, Jeong Y, Kim P, Chun G, Rosa J, Neto AB, Hokka C, Badino A, Kieser T, Bibb M,

1057   Buttner M, Chater K, Hopwood D, Hayes A, Hobbs G, Smith C, Oliver S, Butler P, Evans

1058   C, Herbet D, Tempest D, Takano E, Gramajo H, Strauch E, Andres N, White J, Bibb M,

1059   Bruheim P, Sletta H, Bibb M, White J, Levine D, Hodgson D, Nieselt K, Battke F, Herbig

1060   A, Bruheim P, Wentzel A, Jakobsen O, Sletta H, Alam M, Merlo M, Moore J, Alam M,

1061   Merlo M, Hodgson D, Wellington E, Takano E, Breitling R, Battke F, Symons S, Nieselt K,

1062   Battke F, Herbig A, Wentzel A, Jakobsen O, Bonin M, Hodgson D, Wohlleben W, Ellingsen

1063   T, Nieselt K, Thomas L, Hodgson D, Wentzel A, Nieselt K, Ellingsen T, Moore J, Morrissey

1064   E, Legaie R, Wohlleben W, Rodriguez-Garcia A, Wentzel A, Sletta H, Consortium S,

1065   Ellingsen T, Bruheim P, Waldvogel E, Herbig A, Battke F, Amin R, Nentwich M, Nieselt K,

1066   Ellingsen T, Wentzel A, Hodgson D, Wohlleben W, Mast Y, Claessen D, Rink R, Jong W

1067   de, Siebring J, Vreugd P de, Boersma F, Dijkhuizen L, Wosten H, Bystrykh L, Fernandez-

1068   Moreno M, Herrema J, Malpartida F, Hopwood D, Dijkhuizen L, Villas-Boas S, Delicado

1069   D, Akesson M, Nielsen J, Christensen B, Nielsen J, Strauch E, Takano E, Baylis H, Bibb M,

1070   Martin J, Martin J, Demain A, Coisne S, Béchet M, Blondeau R, Gesheva V, Ivanova V,

1071   Gesheva R, Nakamura T, Yoshimoto A, Rollins M, Jensen S, Westlake D, Gorst-Allman C,

1072   Rudd B, Chang C-J, Floss H, Wasserman H, Shaw C, Sykes R, Cushley R, Bruheim P, Butler

1073   M, Ellingsen T, Jonsbu E, Christensen B, Nielsen J, Gunnarsson N, Bruheim P, Nielsen J,

1074   Rodriguez-Garcia A, Sola-Landa A, Apel K, Santos-Beneit F, Martin J, Santos-Beneit F,

1075   Rodriguez-Garcia A, Sola-Landa A, Martin J, Lambert R, Stratford M, Surowitz K, Pfister

1076   R. 2012. Optimized submerged batch fermentation strategy for systems scale studies of

1077   metabolic switching in Streptomyces coelicolor A3(2). BMC Systems Biology 6:59.

1078   21.   Wentzel A, Sletta H, Consortium S, Ellingsen TE, Bruheim P. 2012. Intracellular

1079   Metabolite Pool Changes in Response to Nutrient Depletion Induced Metabolic

1080   Switching in Streptomyces coelicolor. Metabolites 2:178–194.

1081   22.   Hu H, Zhang Q, Ochi K. 2002. Activation of Antibiotic Biosynthesis by Specified

1082   Mutations in the rpoB Gene (Encoding the RNA Polymerase β Subunit) of Streptomyces

1083   lividans. Journal of Bacteriology 184:3984–3991.

1084   23.   Braesel J, Tran TA, Eustáquio AS. 2019. Heterologous expression of the diazaquinomycin

1085   biosynthetic gene cluster. J Ind Microbiol Biotechnol.

1086   24.   Kepplinger B, Morton-Laing S, Seistrup KH, Marrs ECL, Hopkins AP, Perry JD, Strahl H,

1087   Hall MJ, Errington J, Allenby NEE. 2018. Mode of Action and Heterologous Expression of

1088   the Natural Product Antibiotic Vancoresmycin. ACS Chem Biol 13:207–214.

1089   25.   Li T, Du Y, Cui Q, Zhang J, Zhu W, Hong K, Li W. 2013. Cloning, Characterization and

1090   Heterologous Expression of the Indolocarbazole Biosynthetic Gene Cluster from

1091   Marine-Derived Streptomyces sanyensis FMA. Marine Drugs 11:466–488.

1092   26.   Battke F, Symons S, Nieselt K. 2010. Mayday--integrative analytics for expression data.

1093   BMC Bioinformatics 11:121.

1094   27.   Jäger G, Battke F, Nieselt K. 2011. TIALA — Time series alignment analysis, p. 55–61. *In*

1095   2011 IEEE Symposium on Biological Data Visualization (BioVis).

1096   28.   Liao Y, Smyth GK, Shi W. 2014. featureCounts: an efficient general purpose program for

1097   assigning sequence reads to genomic features. Bioinformatics 30:923–930.

1098   29.   Love MI, Huber W, Anders S. 2014. Moderated estimation of fold change and dispersion

1099   for RNA-seq data with DESeq2. Genome Biol 15:550.

1100   30.   Mi H, Muruganujan A, Ebert D, Huang X, Thomas PD. 2019. PANTHER version 14: more

1101   genomes, a new PANTHER GO-slim and improvements in enrichment analysis tools.

1102   Nucleic Acids Res 47:D419–D426.

1103   31.   Sánchez BJ, Zhang C, Nilsson A, Lahtvee P-J, Kerkhoven EJ, Nielsen J. 2017. Improving

1104   the phenotype predictions of a yeast genome-scale metabolic model by incorporating

1105   enzymatic constraints. Molecular Systems Biology 13:935.

1106   32.   Robinson JL, Nielsen J. 2016. Integrative analysis of human omics data using

1107   biomolecular networks. Mol Biosyst 12:2953–2964.

1108   33.   Borodina I, Krabben P, Nielsen J. 2005. Genome-scale analysis of Streptomyces

1109   coelicolor A3(2) metabolism. Genome research 15:820–9.

1110   34.   Alam MT, Merlo ME, (stream) TSC, Hodgson DA, Wellington EM, Takano E, Breitling R.

1111   2010. Metabolic modeling and analysis of the metabolic switch in Streptomyces

1112   coelicolor. BMC Genomics 11:202.

1113   35.   Amara A, Takano E, Breitling R. 2018. Development and validation of an updated computational model of Streptomyces coelicolor primary and secondary metabolism. BMC Genomics 19:519.

1116   36.   Kim MW, Sang Yi J, Kim J-NJJ-NNJ, Kim J-NJJ-NNJ, Kim MW, Kim B-GG. 2014. Reconstruction of a high-quality metabolic model enables the identification of gene overexpression targets for enhanced antibiotic production in streptomyces coelicolor A3(2). Biotechnology Journal 9:1185–1194.

1120   37.   Wang H, Marcišauskas S, Sánchez BJ, Domenzain I, Hermansson D, Agren R, Nielsen J, Kerkhoven EJ. 2018. RAVEN 2.0: A versatile toolbox for metabolic network reconstruction and a case study on Streptomyces coelicolor. PLOS Computational Biology 14:e1006541.

1124   38.   Mohite OS, Weber T, Kim HU, Lee SY. 2019. Genome-Scale Metabolic Reconstruction of Actinomycetes for Antibiotics Production. Biotechnology Journal 14:1800377.

1126   39.   Toro L, Pinilla L, Avignone-Rossa C, Ríos-Estepa R. 2018. An enhanced genome-scale metabolic reconstruction of Streptomyces clavuligerus identifies novel strain improvement strategies. Bioprocess Biosyst Eng 41:657–669.

1129   40.   Licona-Cassani C, Marcellin E, Quek L-E, Jacob S, Nielsen LK. 2012. Reconstruction of the Saccharopolyspora erythraea genome-scale model and its use for enhancing erythromycin production. Antonie van Leeuwenhoek 102:493–502.

1132   41.   Valverde JR, Gullón S, Mellado RP. 2018. Modelling the metabolism of protein secretion through the Tat route in Streptomyces lividans. BMC Microbiology 18:59.

1134   42.   Lieven C, Beber ME, Olivier BG, Bergmann FT, Ataman M, Babaei P, Bartell JA, Blank LM,

1135   Chauhan S, Correia K, Diener C, Dräger A, Ebert BE, Edirisinghe JN, Faria JP, Feist A,

1136   Fengos G, Fleming RMT, Garcia-Jimenez B, Hatzimanikatis V, Helvoirt W van, Henry C,

1137   Hermjakob H, Herrgard MJ, Kim HU, King Z, Koehorst JJ, Klamt S, Klipp E, Lakshmanan

1138   M, Novere NL, Lee D-Y, Lee SY, Lee S, Lewis NE, Ma H, Machado D, Mahadevan R, Maia

1139   P, Mardinoglu A, Medlock GL, Monk J, Nielsen J, Nielsen LK, Nogales J, Nookaew I,

1140   Resendis O, Palsson B, Papin JA, Patil KR, Poolman M, Price ND, Richelle A, Rocha I,

1141   Sanchez B, Schaap P, Sheriff RSM, Shoaie S, Sonnenschein N, Teusink B, Vilaca P, Vik JO,

1142   Wodke JA, Xavier JC, Yuan Q, Zakhartsev M, Zhang C. 2018. Memote: A community-

1143   driven effort towards a standardized genome-scale metabolic model test suite. bioRxiv

1144   350991.

1145   43.   Thiele I, Swainston N, Fleming RMT, Hoppe A, Sahoo S, Aurich MK, Haraldsdottir H, Mo

1146   ML, Rolfsson O, Stobbe MD, Thorleifsson SG, Agren R, Bölling C, Bordel S, Chavali AK,

1147   Dobson P, Dunn WB, Endler L, Hala D, Hucka M, Hull D, Jameson D, Jamshidi N, Jonsson

1148   JJ, Juty N, Keating S, Nookaew I, Le Novère N, Malys N, Mazein A, Papin JA, Price ND,

1149   Selkov E, Sigurdsson MI, Simeonidis E, Sonnenschein N, Smallbone K, Sorokin A, van

1150   Beek JHGM, Weichart D, Goryanin I, Nielsen J, Westerhoff HV, Kell DB, Mendes P,

1151   Palsson BØ. 2013. A community-driven global reconstruction of human metabolism.

1152   Nat Biotechnol 31.

1153   44.   Aung HW, Henry SA, Walker LP. 2013. Revising the Representation of Fatty Acid,

1154   Glycerolipid, and Glycerophospholipid Metabolism in the Consensus Model of Yeast

1155   Metabolism. Industrial Biotechnology 9:215–228.

1156   45.   Dobson PD, Smallbone K, Jameson D, Simeonidis E, Lanthaler K, Pir P, Lu C, Swainston

1157   N, Dunn WB, Fisher P, Hull D, Brown M, Oshota O, Stanford NJ, Kell DB, King RD, Oliver

1158   SG, Stevens RD, Mendes P. 2010. Further developments towards a genome-scale

1159   metabolic model of yeast. BMC Syst Biol 4:145.

1160   46.   Heavner BD, Smallbone K, Barker B, Mendes P, Walker LP. 2012. Yeast 5 – an expanded

1161   reconstruction of the Saccharomyces cerevisiae metabolic network. BMC Systems

1162   Biology 6:55.

1163   47.   Heavner BD, Smallbone K, Price ND, Walker LP. 2013. Version 6 of the consensus yeast

1164   metabolic network refines biochemical coverage and improves model performance.

1165   Database (Oxford) 2013:bat059.

1166   48.   Herrgård MJ, Swainston N, Dobson P, Dunn WB, Arga KY, Arvas M, Blüthgen N, Borger

1167   S, Costenoble R, Heinemann M, Hucka M, Le Novère N, Li P, Liebermeister W, Mo ML,

1168   Oliveira AP, Petranovic D, Pettifer S, Simeonidis E, Smallbone K, Spasić I, Weichart D,

1169   Brent R, Broomhead DS, Westerhoff HV, Kırdar B, Penttilä M, Klipp E, Palsson BØ, Sauer

1170   U, Oliver SG, Mendes P, Nielsen J, Kell DB. 2008. A consensus yeast metabolic network

1171   reconstruction obtained from a community approach to systems biology. Nat

1172   Biotechnol 26:1155–1160.

1173   49.   Lu H, Li F, Sánchez BJ, Zhu Z, Li G, Domenzain I, Marcišauskas S, Anton PM, Lappa D,

1174   Lieven C, Beber ME, Sonnenschein N, Kerkhoven EJ, Nielsen J. 2019. A consensus S.

1175   cerevisiae metabolic model Yeast8 and its ecosystem for comprehensively probing

1176   cellular metabolism. Nat Commun 10:1–13.

1177   50.   Hefzi H, Ang KS, Hanscho M, Bordbar A, Ruckerbauer D, Lakshmanan M, Orellana CA,

1178   Baycin-Hizal D, Huang Y, Ley D, Martinez VS, Kyriakopoulos S, Jiménez NE, Zielinski DC,

1179   Quek L-E, Wulff T, Arnsdorf J, Li S, Lee JS, Paglia G, Loira N, Spahn PN, Pedersen LE,

1180   Gutierrez JM, King ZA, Lund AM, Nagarajan H, Thomas A, Abdel-Haleem AM, Zanghellini

1181   J, Kildegaard HF, Voldborg BG, Gerdtzen ZP, Betenbaugh MJ, Palsson BO, Andersen MR,

1182   Nielsen LK, Borth N, Lee D-Y, Lewis NE. 2016. A Consensus Genome-scale

1183   Reconstruction of Chinese Hamster Ovary Cell Metabolism. Cell Systems 3:434-443.e8.

1184   51.   Kanehisa M. 2000. KEGG: Kyoto Encyclopedia of Genes and Genomes. Nucleic Acids

1185   Research 28:27–30.

1186   52.   Kanehisa M, Sato Y, Furumichi M, Morishima K, Tanabe M. 2019. New approach for

1187   understanding genome variations in KEGG. Nucleic Acids Research 47:D590–D595.

1188   53.   Karp PD, Billington R, Caspi R, Fulcher CA, Latendresse M, Kothari A, Keseler IM,

1189   Krummenacker M, Midford PE, Ong Q, Ong WK, Paley SM, Subhraveti P. 2017. The

1190   BioCyc collection of microbial genomes and metabolic pathways. Brief Bioinform.

1191   54.   Hastings J, Owen G, Dekker A, Ennis M, Kale N, Muthukrishnan V, Turner S, Swainston

1192   N, Mendes P, Steinbeck C. 2016. ChEBI in 2016: Improved services and an expanding

1193   collection of metabolites. Nucleic Acids Res 44:D1214–D1219.

1194   55.   Moretti S, Martin O, Van Du Tran T, Bridge A, Morgat A, Pagni M. 2016.

1195   MetaNetX/MNXref – reconciliation of metabolites and biochemical reactions to bring

1196   together genome-scale metabolic networks. Nucleic Acids Res 44:D523–D526.

1197   56.   King ZA, Lu J, Dräger A, Miller P, Federowicz S, Lerman JA, Ebrahim A, Palsson BO, Lewis

1198   NE, J. H. 2016. BiGG Models: A platform for integrating, standardizing and sharing

1199   genome-scale models. Nucleic Acids Research 44:D515–D522.

1200   57.   The UniProt Consortium. 2019. UniProt: a worldwide hub of protein knowledge. Nucleic

1201   Acids Res 47:D506–D515.

1202   58.   Thiele I, Palsson BØ. 2010. A protocol for generating a high-quality genome-scale

1203   metabolic reconstruction. Nature protocols 5:93–121.

1204   59.   Flamholz A, Noor E, Bar-Even A, Milo R. 2012. eQuilibrator—the biochemical

1205   thermodynamics calculator. Nucleic Acids Res 40:D770–D775.

1206   60.   Chakrabarty AM. 1998. Nucleoside diphosphate kinase: role in bacterial growth,

1207   virulence, cell signalling and polysaccharide synthesis. Molecular Microbiology 28:875–

1208   882.

1209   61.   Yoshida M, Muneyuki E, Hisabori T. 2001. ATP synthase — a marvellous rotary engine

1210   of the cell. Nat Rev Mol Cell Biol 2:669–677.

1211   62.   Getsin I, Nalbandian GH, Yee DC, Vastermark A, Paparoditis PC, Reddy VS, Saier MH.

1212   2013. Comparative genomics of transport proteins in developmental bacteria:

1213   Myxococcus xanthus and Streptomyces coelicolor. BMC Microbiol 13:279.

1214   63.   Smirnov A, Esnault C, Prigent M, Holland IB, Virolle M-J. 2015. Phosphate Homeostasis

1215   in Conditions of Phosphate Proficiency and Limitation in the Wild Type and the phoP

1216   Mutant of Streptomyces lividans. PLoS One 10.

1217   64.   Orth JD, Thiele I, Palsson BØO. 2010. What is flux balance analysis? Nat Biotech 28:245–

1218   248.

1219   65.   Bordel S, Agren R, Nielsen J. 2010. Sampling the Solution Space in Genome-Scale

1220   Metabolic Networks Reveals Transcriptional Regulation in Key Enzymes. PLOS

1221   Computational Biology 6:e1000859.

1222   66.   Martín JF, Santos-Beneit F, Rodríguez-García A, Sola-Landa A, Smith MCM, Ellingsen TE,

1223   Nieselt K, Burroughs NJ, Wellington EMH. 2012. Transcriptomic studies of phosphate

1224   control of primary and secondary metabolism in Streptomyces coelicolor. Appl

1225   Microbiol Biotechnol 95:61–75.

1226   67.   Martín-Martín S, Rodríguez-García A, Santos-Beneit F, Franco-Domínguez E, Sola-Landa

1227   A, Martín JF. 2018. Self-control of the PHO regulon: the PhoP-dependent protein PhoU

1228   controls negatively expression of genes of PHO regulon in *Streptomyces coelicolor*. The

1229   Journal of Antibiotics 71:113–122.

1230   68.   Sola-Landa A, Moura RS, Martín JF. 2003. The two-component PhoR-PhoP system

1231   controls both primary metabolism and secondary metabolite biosynthesis in

1232   Streptomyces lividans. Proc Natl Acad Sci U S A 100:6133–6138.

1233   69.   Martín JF, Rodríguez-García A, Liras P. 2017. The master regulator PhoP coordinates

1234   phosphate and nitrogen metabolism, respiration, cell differentiation and antibiotic

1235   biosynthesis: comparison in *Streptomyces coelicolor* and *Streptomyces avermitilis*. The

1236   Journal of Antibiotics 70:534–541.

1237   70.   Li L, Jiang W, Lu Y. 2017. A Novel Two-Component System, GluR-GluK, Involved in

1238   Glutamate Sensing and Uptake in Streptomyces coelicolor. Journal of Bacteriology 199.

1239   71.   Fink D, Weißschuh N, Reuther J, Wohlleben W, Engels A. 2002. Two transcriptional

1240   regulators GlnR and GlnRII are involved in regulation of nitrogen metabolism in

1241   *Streptomyces coelicolor* A3(2). Molecular Microbiology 46:331–347.

1242   72.   Martín JF. 2004. Phosphate Control of the Biosynthesis of Antibiotics and Other

1243   Secondary Metabolites Is Mediated by the PhoR-PhoP System: an Unfinished Story.

1244   Journal of Bacteriology 186:5197–5201.

1245   73.   Stirrett K, Denoya C, Westpheling J. 2009. Branched-chain amino acid catabolism

1246   provides precursors for the Type II polyketide antibiotic, actinorhodin, via pathways

1247   that are nutrient dependent. J Ind Microbiol Biotechnol 36:129–137.

1248   74.   Esnault C, Dulermo T, Smirnov A, Askora A, David M, Deniset-Besseau A, Holland I-B,

1249   Virolle M-J. 2017. Strong antibiotic production is correlated with highly active oxidative

1250   metabolism in Streptomyces coelicolor M145. Scientific Reports 7:200.

1251   75.   Borodina I, Siebring J, Zhang J, Smith CP, Keulen G van, Dijkhuizen L, Nielsen J. 2008.

1252   Antibiotic   Overproduction   in   Streptomyces   coelicolor   A3(2)   Mediated   by

1253   Phosphofructokinase Deletion. J Biol Chem 283:25186–25199.

1254   76.   Jonsbu E, Christensen B, Nielsen J. 2001. Changes of in vivo fluxes through central

1255   metabolic pathways during the production of nystatin by Streptomyces noursei in batch

1256   culture. Appl Microbiol Biotechnol 56:93–100.

1257   77.   Gallo G, Renzone G, Alduina R, Stegmann E, Weber T, Lantz AE, Thykaer J, Sangiorgi F,

1258   Scaloni A, Puglia AM. 2010. Differential proteomic analysis reveals novel links between

1259   primary metabolism and antibiotic production in Amycolatopsis balhimycina.

1260   PROTEOMICS 10:1336–1358.

1261   78.   Coze F, Gilard F, Tcherkez G, Virolle M-J, Guyonvarch A. 2013. Carbon-Flux Distribution

1262   within Streptomyces coelicolor Metabolism: A Comparison between the Actinorhodin-

1263   Producing Strain M145 and Its Non-Producing Derivative M1146. PLOS ONE 8:e84151.

1264   79.   Millan-Oropeza A, Henry C, Blein-Nicolas M, Aubert-Frambourg A, Moussa F, Bleton J,

1265   Virolle M-J. 2017. Quantitative Proteomics Analysis Confirmed Oxidative Metabolism

1266   Predominates in Streptomyces coelicolor versus Glycolytic Metabolism in Streptomyces

1267   lividans. J Proteome Res 16:2597–2613.

1268   80.   Ashburner M, Ball CA, Blake JA, Botstein D, Butler H, Cherry JM, Davis AP, Dolinski K,

1269   Dwight SS, Eppig JT, Harris MA, Hill DP, Issel-Tarver L, Kasarskis A, Lewis S, Matese JC,

1270   Richardson JE, Ringwald M, Rubin GM, Sherlock G. 2000. Gene ontology: tool for the

1271   unification of biology. The Gene Ontology Consortium. Nat Genet 25:25–29.

1272   81.   The Gene Ontology Consortium. 2019. The Gene Ontology Resource: 20 years and still

1273   GOing strong. Nucleic Acids Res 47:D330–D338.

1274   82.   Stahl W, Sies H. 2003. Antioxidant activity of carotenoids. Molecular Aspects of

1275   Medicine 24:345–351.

1276   83.   Latifi A, Ruiz M, Zhang C-C. 2009. Oxidative stress in cyanobacteria. FEMS Microbiol Rev

1277   33:258–278.

1278   84.   Zangar RC, Davydov DR, Verma S. 2004. Mechanisms that regulate production of reactive oxygen species by cytochrome P450. Toxicology and Applied Pharmacology 199:316–331.

1281   85.   Lamb DC, Ikeda H, Nelson DR, Ishikawa J, Skaug T, Jackson C, Omura S, Waterman MR, Kelly SL. 2003. Cytochrome P450 complement (CYPome) of the avermectin-producer Streptomyces avermitilis and comparison to that of Streptomyces coelicolor A3(2). Biochemical and Biophysical Research Communications 307:610–619.

1285   86.   Bednarz B, Kotowska M, Pawlik KJ. 2019. Multi-level regulation of coelimycin synthesis in Streptomyces coelicolor A3(2). Appl Microbiol Biotechnol 103:6423–6434.

1287   87.   Li X, Wang J, Li S, Ji J, Wang W, Yang K. 2015. ScbR- and ScbR2-mediated signal transduction networks coordinate complex physiological responses in *Streptomyces coelicolor*. Scientific Reports 5:14831.

1290   88.   Lee P-C, Umeyama T, Horinouchi S. 2002. afsS is a target of AfsR, a transcriptional factor with ATPase activity that globally controls secondary metabolism in Streptomyces coelicolor A3(2). Molecular Microbiology 43:1413–1430.

1293   89.   Horinouchi S. 2003. AfsR as an integrator of signals that are sensed by multiple serine/threonine kinases in Streptomyces coelicolor A3(2). J IND MICROBIOL BIOTECHNOL 30:462–467.

1296   90.   Naseer N, Shapiro JA, Chander M. 2014. RNA-Seq analysis reveals a six-gene SoxR regulon in Streptomyces coelicolor. PLoS ONE 9:e106181.

1298   91.   Dela Cruz R, Gao Y, Penumetcha S, Sheplock R, Weng K, Chander M. 2010. Expression

1299   of the Streptomyces coelicolor SoxR regulon is intimately linked with actinorhodin

1300   production. J Bacteriol 192:6428–6438.

1301   92.   Shin J-H, Singh AK, Cheon D-J, Roe J-H. 2011. Activation of the SoxR regulon in

1302   Streptomyces coelicolor by the extracellular form of the pigmented antibiotic

1303   actinorhodin. J Bacteriol 193:75–81.

1304   93.   Valton J, Mathevon C, Fontecave M, Nivière V, Ballou DP. 2008. Mechanism and

1305   regulation of the Two-component FMN-dependent monooxygenase ActVA-ActVB from

1306   Streptomyces coelicolor. J Biol Chem 283:10287–10296.

1307   94.   Burgos HL, O'Connor K, Sanchez-Vazquez P, Gourse RL. 2017. Roles of Transcriptional

1308   and Translational Control Mechanisms in Regulation of Ribosomal Protein Synthesis in

1309   Escherichia coli. J Bacteriol 199.

1310   95.   Hesketh A, Chen WJ, Ryding J, Chang S, Bibb M. 2007. The global role of ppGpp synthesis

1311   in morphological differentiation and antibiotic production in Streptomyces coelicolor

1312   A3(2). Genome Biol 8:R161.

1313   96.   Srivatsan A, Wang JD. 2008. Control of bacterial transcription, translation and

1314   replication by (p)ppGpp. Current Opinion in Microbiology 11:100–105.

1315   97.   Gaal T, Bartlett MS, Ross W, Turnbough CL, Gourse RL. 1997. Transcription Regulation

1316   by Initiating NTP Concentration: rRNA Synthesis in Bacteria. Science 278:2092–2097.

1317   98.   Chemler JA, Buchholz TJ, Geders TW, Akey DL, Rath CM, Chlipala GE, Smith JL, Sherman

1318   DH. 2012. Biochemical and Structural Characterization of Germicidin Synthase: Analysis

1319   of a Type III Polyketide Synthase that Employs Acyl-ACP as a Starter Unit Donor. J Am

1320   Chem Soc 134:7359–7366.

1321 99. Xu J, Tozawa Y, Lai C, Hayashi H, Ochi K. 2002. A rifampicin resistance mutation in the

1322   rpoB gene confers ppGpp-independent antibiotic production in Streptomyces coelicolor

1323   A3(2). Mol Gen Genomics 268:179–189.

1324 100. Craney A, Ozimok C, Pimentel-Elardo SM, Capretta A, Nodwell JR. 2012. Chemical

1325   Perturbation of Secondary Metabolism Demonstrates Important Links to Primary

1326   Metabolism. Chemistry & Biology 19:1020–1027.

1327 101. Courtot M, Juty N, Knüpfer C, Waltemath D, Zhukova A, Dräger A, Dumontier M, Finney

1328   A, Golebiewski M, Hastings J, Hoops S, Keating S, Kell DB, Kerrien S, Lawson J, Lister A,

1329   Lu J, Machne R, Mendes P, Pocock M, Rodriguez N, Villeger A, Wilkinson DJ,

1330   Wimalaratne S, Laibe C, Hucka M, Le Novère N. 2011. Controlled vocabularies and

1331   semantics in systems biology. Mol Syst Biol 7:543.

1332 102. Noor E, Haraldsdóttir HS, Milo R, Fleming RMT. 2013. Consistent Estimation of Gibbs

1333   Energy Using Component Contributions. PLOS Computational Biology 9:e1003098.

1334 103. Bar-Even A, Flamholz A, Noor E, Milo R. 2012. Thermodynamic constraints shape the

1335   structure of carbon fixation pathways. Biochimica et Biophysica Acta (BBA) -

1336   Bioenergetics 1817:1646–1659.

1337 104. Feist AM, Henry CS, Reed JL, Krummenacker M, Joyce AR, Karp PD, Broadbelt LJ,

1338   Hatzimanikatis V, Palsson BØ. 2007. A genome-scale metabolic reconstruction for

Escherichia coli K-12 MG1655 that accounts for 1260 ORFs and thermodynamic information. Molecular Systems Biology 3:121.

105. Elbourne LDH, Tetu SG, Hassan KA, Paulsen IT. 2017. TransportDB 2.0: a database for exploring membrane transporters in sequenced genomes from all domains of life. Nucleic Acids Research 45:D320–D324.

106. Saier MH, Reddy VS, Tsu BV, Ahmed MS, Li C, Moreno-Hagelsieb G. 2016. The Transporter Classification Database (TCDB): recent advances. Nucleic Acids Res 44:D372–D379.

107. NCBI Resource Coordinators. 2017. Database Resources of the National Center for Biotechnology Information. Nucleic Acids Research 45:D12–D17.

108. Jeske L, Placzek S, Schomburg I, Chang A, Schomburg D. 2019. BRENDA in 2019: a European ELIXIR core data resource. Nucleic Acids Res 47:D542–D549.

109. Fritzemeier CJ, Hartleb D, Szappanos B, Papp B, Lercher MJ. 2017. Erroneous energy-generating cycles in published genome scale metabolic networks: Identification and removal. PLOS Computational Biology 13:e1005494.

110. Noor E. 2018. Removing both Internal and Unrealistic Energy-Generating Cycles in Flux Balance Analysis. arXiv:180304999 [q-bio].

111. Haraldsdóttir HS, Cousins B, Thiele I, Fleming RMT, Vempala S. 2017. CHRR: coordinate hit-and-run with rounding for uniform sampling of constraint-based models. Bioinformatics 33:1741–1743.

1359   112.   Kaufman DE, Smith RL. 1998. Direction Choice for Accelerated Convergence in Hit-and-

1360   Run Sampling. Operations Research 46:84–95.

1361   113.   Megchelenbrink W, Huynen M, Marchiori E. 2014. optGpSampler: An Improved Tool for

1362   Uniformly Sampling the Solution-Space of Genome-Scale Metabolic Networks. PLOS

1363   ONE 9:e86587.

1364   114.   Kieser T, Bibb MJ, Buttner M, Chater K, Hopwood DA. 2000. Practical Streptomyces

1365   Genetics. John Innes Foundation, Norwich, UK.

1366   115.   Claessen D, Rink R, Jong W de, Siebring J, Vreugd P de, Boersma FGH, Dijkhuizen L,

1367   Wösten HAB. 2003. A novel class of secreted hydrophobic proteins is involved in aerial

1368   hyphae formation in Streptomyces coelicolor by forming amyloid-like fibrils. Genes Dev

1369   17:1714–1726.

1370   116.   Bystrykh LV, Fernández-Moreno MA, Herrema JK, Malpartida F, Hopwood DA,

1371   Dijkhuizen L. 1996. Production of actinorhodin-related "blue pigments" by

1372   Streptomyces coelicolor A3(2). J Bacteriol 178:2238–2244.

1373   117.   Gubbens J, Janus M, Florea BI, Overkleeft HS, van Wezel GP. 2012. Identification of

1374   glucose kinase-dependent and -independent pathways for carbon control of primary

1375   metabolism, development and antibiotic production in *Streptomyces coelicolor* by

1376   quantitative proteomics. Molecular Microbiology 86:1490–1507.

1377   118.   Wessel D, Flügge UI. 1984. A method for the quantitative recovery of protein in dilute

1378   solution in the presence of detergents and lipids. Anal Biochem 138:141–143.

1379   119. Rappsilber J, Mann M, Ishihama Y. 2007. Protocol for micro-purification, enrichment,

1380   pre-fractionation and storage of peptides for proteomics using StageTips. Nat Protoc

1381   2:1896–1906.

1382   120. Distler U, Kuharev J, Navarro P, Levin Y, Schild H, Tenzer S. 2014. Drift time-specific

1383   collision energies enable deep-coverage data-independent acquisition proteomics. Nat

1384   Methods 11:167–170.

1385   121. Andrews S. 2016. FastQC: a quality control tool for high throughput sequence data.

1386   122. Kim D, Langmead B, Salzberg SL. 2015. HISAT: a fast spliced aligner with low memory

1387   requirements. Nat Methods 12:357–360.

1388   123. Li H, Handsaker B, Wysoker A, Fennell T, Ruan J, Homer N, Marth G, Abecasis G, Durbin

1389   R, 1000 Genome Project Data Processing Subgroup. 2009. The Sequence

1390   Alignment/Map format and SAMtools. Bioinformatics 25:2078–2079.

1391   124. Okonechnikov K, Conesa A, García-Alcalde F. 2016. Qualimap 2: advanced multi-sample

1392   quality control for high-throughput sequencing data. Bioinformatics 32:292–294.

1393   125. Battke F, Nieselt K. 2011. Mayday SeaSight: combined analysis of deep sequencing and

1394   microarray data. PLoS ONE 6:e16345.

1395   126. Huang DW, Sherman BT, Lempicki RA. 2009. Bioinformatics enrichment tools: paths

1396   toward the comprehensive functional analysis of large gene lists. Nucleic Acids Res

1397   37:1–13.

1398   127. Huang DW, Sherman BT, Lempicki RA. 2009. Systematic and integrative analysis of large

1399   gene lists using DAVID bioinformatics resources. Nat Protoc 4:44–57.

1400   128. Szklarczyk D, Gable AL, Lyon D, Junge A, Wyder S, Huerta-Cepas J, Simonovic M,

1401   Doncheva NT, Morris JH, Bork P, Jensen LJ, Mering C von. 2019. STRING v11: protein-

1402   protein association networks with increased coverage, supporting functional discovery

1403   in genome-wide experimental datasets. Nucleic Acids Res 47:D607–D613.

1404   129. Perez-Riverol Y, Csordas A, Bai J, Bernal-Llinares M, Hewapathirana S, Kundu DJ,

1405   Inuganti A, Griss J, Mayer G, Eisenacher M, Pérez E, Uszkoreit J, Pfeuffer J, Sachsenberg

1406   T, Yilmaz S, Tiwary S, Cox J, Audain E, Walzer M, Jarnuczak AF, Ternent T, Brazma A,

1407   Vizcaíno JA. 2019. The PRIDE database and related tools and resources in 2019:

1408   improving support for quantification data. Nucleic Acids Res 47:D442–D450.

1409

1410